


TUTORIAL

Protein functional dynamics from the rigorous global analysis of DEER data: Conditions, components, and conformations

Eric J. Hustedt¹ , Richard A. Stein¹, and Hassane S. Mchaourab¹ 

The potential of spin labeling to reveal the dynamic dimension of macromolecules has been recognized since the dawn of the methodology in the 1960s. However, it was the development of pulsed electron paramagnetic resonance spectroscopy to detect dipolar coupling between spin labels and the availability of turnkey instrumentation in the 21st century that realized the full promise of spin labeling. Double electron-electron resonance (DEER) spectroscopy has seen widespread applications to channels, transporters, and receptors. In these studies, distance distributions between pairs of spin labels obtained under different biochemical conditions report the conformational states of macromolecules, illuminating the key movements underlying biological function. These experimental studies have spurred the development of methods for the rigorous analysis of DEER spectroscopic data along with methods for integrating these distributions into structural models. In this tutorial, we describe a model-based approach to obtaining a minimum set of components of the distance distribution that correspond to functionally relevant protein conformations with a set of fractional amplitudes that define the equilibrium between these conformations. Importantly, we review and elaborate on the error analysis reflecting the uncertainty in the various parameters, a critical step in rigorous structural interpretation of the spectroscopic data.

Introduction

The modern tool kit of structural biology includes diverse, complementary methods spanning the spectrum from computational to experimental that can visualize global structures at atomic resolution as well as probe them on local site-specific levels and can reveal the dynamic dimension under equilibrium or time-resolved conditions. The integration of these methods has been touted as the next frontier in the quest to reveal the interplay of structure and dynamics that underpins protein function. Probe methods, including electron paramagnetic resonance (EPR) spectroscopy of site-specifically spin-labeled proteins, have contributed a unique perspective on protein dynamics (Mchaourab et al., 2011; Claxton et al., 2015; Jeschke, 2018a). In particular, pulsed EPR methods are distinguished by the ability to investigate proteins in multiple conformational states in near-native environments with high sensitivity. Because integration of structural biology data is mostly performed a posteriori, the process requires not only knowledge of the rules of interpretation (i.e., how models are derived from data) but also well-established tools for assessment of rigor and reproducibility of the underlying analysis.

The pulsed EPR technique double electron-electron resonance (DEER) spectroscopy measures long-range (>20 Å)

distances between electron spins (Jeschke, 2012; Borbat and Freed, 2014; Jeschke, 2014), typically extrinsic probes introduced into biological macromolecules by site-directed spin labeling (Roser et al., 2016). DEER has been applied to multiple proteins, RNA, and DNA systems. In the protein space, unique insight was revealed on ion channel architecture and gating (Pliotas et al., 2012; Dellisanti et al., 2013; Dalmas et al., 2014; Dürr et al., 2014; Puljung et al., 2014; Raghuraman et al., 2014; Arrigoni et al., 2016; Zhu et al., 2016; Evans et al., 2020), transporter alternating access and energy landscapes (Claxton et al., 2010; Mittal et al., 2012; Georgieva et al., 2013; Kazmier et al., 2014a; Kazmier et al., 2014b; Masureel et al., 2014; Joseph et al., 2015; Dastvan et al., 2016; Martens et al., 2016; Timachi et al., 2017; Verhalen et al., 2017; Göddeke et al., 2018; Dastvan et al., 2019; Joseph et al., 2019; Nyenhuis et al., 2020), and receptor activation and allosteric modulation (Park et al., 2006; Kim et al., 2012; Kang et al., 2015; Yee et al., 2015; Van Eps et al., 2017; Van Eps et al., 2018; Wingler et al., 2019; Elgeti and Hubbell, 2021). The range of applications of DEER include evaluation of static structures in solution (e.g., Zhou et al., 2005) or native-like environments (e.g., Barrett et al., 2012), probing ligand-induced conformational changes, characterization

¹Molecular Physiology and Biophysics, Vanderbilt University School of Medicine, Nashville, TN.

Correspondence to Eric J. Hustedt: eric.hustedt@vanderbilt.edu; Hassane S. Mchaourab: hassane.mchaourab@vanderbilt.edu.

© 2021 Hustedt et al. This article is distributed under the terms of an Attribution–Noncommercial–Share Alike–No Mirror Sites license for the first six months after the publication date (see <http://www.rupress.org/terms/>). After six months it is available under a Creative Commons License (Attribution–Noncommercial–Share Alike 4.0 International license, as described at <https://creativecommons.org/licenses/by-nc-sa/4.0/>).

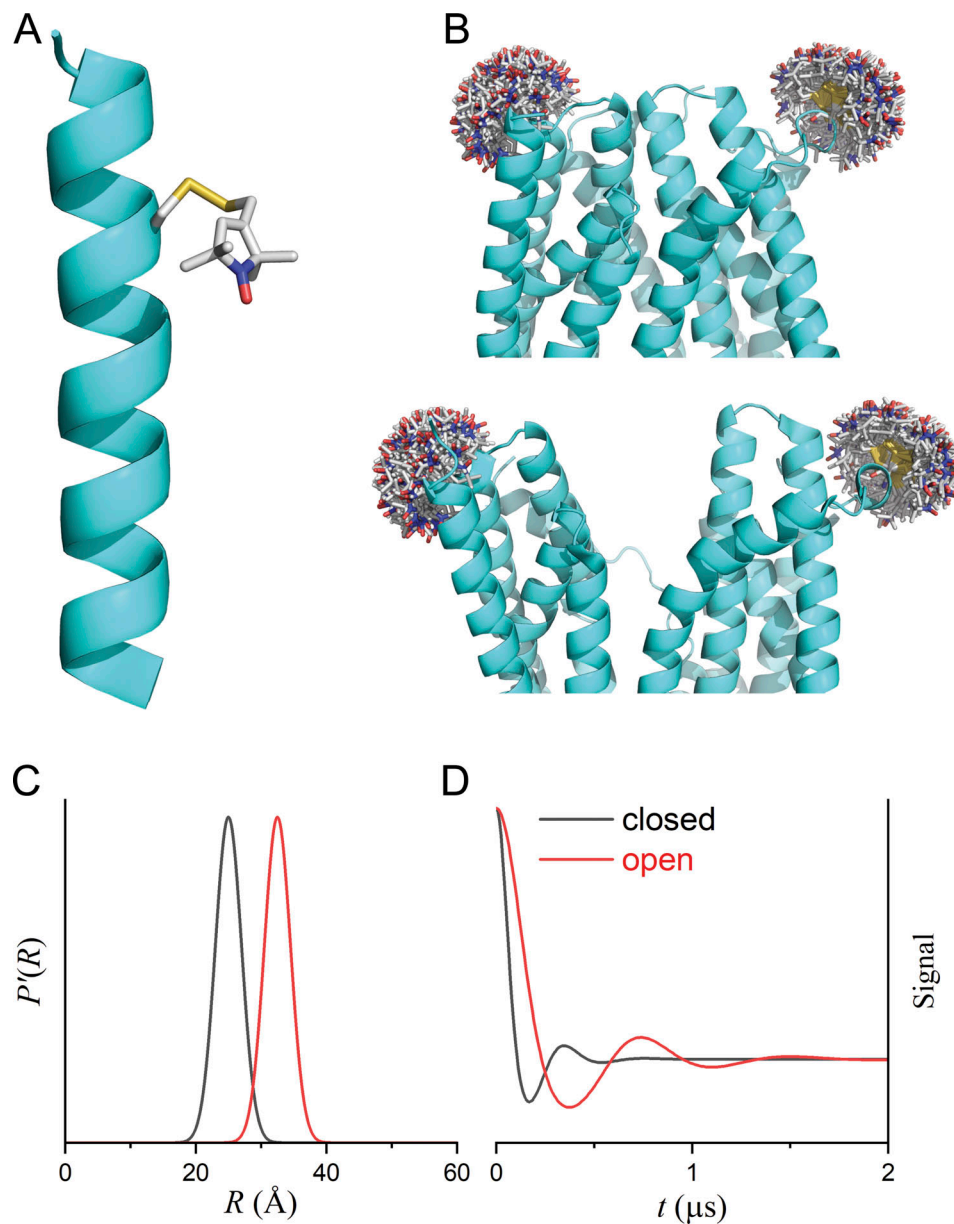


Figure 1. **Site-directed spin labeling and DEER.** (A) Model showing the MTSSL attached to an α -helix at a cysteine residue. (B) Models showing spin labels at extracellular sites of two helices of an integral membrane protein in two different conformational states. (C) The expected distance distributions for the OO (red) and OC (black) states. (D) The corresponding intramolecular DEER signals.

of equilibrium fluctuations, and investigation of protein–protein interactions (Hilger et al., 2005; Hilger et al., 2007; Kim et al., 2011; Edwards et al., 2014). The most frequent strategy is to attach pairs of spin labels at introduced cysteines in a purified protein (Fig. 1 A), although promising alternative strategies have been introduced (Roser et al., 2016; Ackermann et al., 2021; Gamble Jarvi et al., 2021). Multiple pairs are designed to provide a pattern of characteristic distances or distance changes relevant to the structure or model to be tested. Distance restraints from DEER have been integrated with computation methods to model protein structures ab initio (Alexander et al., 2008; Alexander et al., 2013; Jeschke, 2016), to refine structures, and to generate models of intermediate states (Kazmier et al., 2014b; Evans et al., 2020) or protein complexes (Kim

et al., 2012; Edwards et al., 2014). In combination with cryo-EM, DEER distance distributions can provide a complementary approach to pinpoint the mechanistic identity of various conformations and to validate models of conformational changes (Dürr et al., 2014; Zhu et al., 2016).

The cornerstones of DEER data interpretation are the rigorous transformation of the raw signals into complex distance distributions, the structural interpretation of these distributions as spatial restraints, and the generation of structural models consistent with the derived restraints. As an illustration, consider a hypothetical membrane transporter doubly labeled at the extracellular surface of two transmembrane (TM) helices (Fig. 1 B) with two conformations, outward closed (OC) and outward open (OO), that differ by a large translocation of one helix

relative to the other. The distribution, P , of distances, R , between the labels for each conformation (Fig. 1 C) is determined by its tertiary structures, the degree of disorder in the structure, and the rotameric disorder of the labels. The different distance distributions for the two conformations produce distinct DEER time traces (Fig. 1 D).

More generally, distinct distance components with varying widths in the $P(R)$ reflect the collection of conformations of the protein backbone that are populated under the experimental conditions and the rotameric states of the spin-label side chain at each of these conformations. Biochemical conditions can be manipulated to shift the energies of protein conformers, leading to a set of DEER signal traces that differ by the populations of these components. Here, we focus on tools for the rigorous analysis of multiple DEER time traces obtained under varying conditions from one or more doubly spin-labeled mutants of a given protein. We describe a model-based approach to obtaining a minimum set of distance components related to functionally relevant conformations with a set of fractional amplitudes that define the equilibrium between these conformations together with error analysis reflecting the uncertainty in the various parameters.

From DEER signal to distance distribution

Much work has been devoted to the development of methods for the analysis of DEER data to determine the optimal $P(R)$. Broadly, these methods can be described as either model based, expressing the $P(R)$ as a linear combination of components (typically Gaussian), or model free, often using a mathematical regularization method. A DEER time-domain experimental signal, $V(t)$, is the product of a signal, $V_O(t)$, arising from the dipolar interactions within a labeled molecule or complex and a background signal, $V_B(t)$, arising from intermolecular dipolar interactions (Pannier et al., 2000b; Bowman et al., 2004).

$$V(t) = V_O(t) \times V_B(t) + \epsilon(t) \quad (1)$$

where $\epsilon(t)$ is random noise drawn from a normal distribution whose variance is independent of t (Edwards and Stoll, 2016). Typically, nitroxide spin labels are sufficiently disordered (see Fig. 1 B) to eliminate correlation between the interspin distance and relative orientation eliminating any orientation selection effects (Polyhach et al., 2007; Schiemann et al., 2009). After averaging over all possible relative orientations, the intramolecular signal, which is the signal of interest, can be modeled as follows:

$$O(t) = (1 - \Delta) + \Delta \int_0^\infty G(\omega_d(R)t) P(R) dR \quad (2)$$

The modulation depth, Δ , is a function of both the labeling efficiency and various instrumental factors. $G(\omega_d(R)t)$ has been previously defined (Milov et al., 1998; Bowman et al., 2004; Edwards and Stoll, 2016):

$$G(\omega_d t) = \frac{\sqrt{C^2 + S^2}}{\kappa} \cos\left(\omega_d t - \tan^{-1} \frac{S}{C}\right) = \frac{C}{\kappa} \cos(\omega_d t) + \frac{S}{\kappa} \sin(\omega_d t), \quad (3)$$

where C and S are the Fresnel cosine and sine integrals

$$\begin{aligned} C &= \int_0^\kappa \cos \frac{\pi}{2} x^2 dx \\ S &= \int_0^\kappa \sin \frac{\pi}{2} x^2 dx \\ \kappa &= \sqrt{\frac{6\omega_d t}{\pi}} \\ \omega_d &= \frac{g^2 \mu_B^2 \mu_0}{4\pi\hbar} \frac{1}{R^3}, \end{aligned} \quad (4)$$

and the symbols in the equation for the dipolar frequency, ω_d , represent the usual physical constants.

The background factor can be modeled as an exponential, a stretched exponential function (Milov et al., 1998),

$$B(t) = e^{(-10^n |t|)^d} \quad (5)$$

or any other desired model including one that accounts for an excluded volume effect (Brandon et al., 2012; Kattinig et al., 2013). All data in this work has been fit with a pure exponential background factor ($d = 3$) corresponding to a 3-D homogeneous solution. The use of an exponential expression, 10^n , to parameterize the background decay rate reduces the dynamic range of the fit parameter and can improve fitting. For a homogeneous 3-D solution of spins ($d = 3$), an effective spin concentration can be calculated from the background decay rate (see Appendix).

Model-based analysis of DEER data assumes that $P(R)$ can be described by a sum of n components:

$$P(R) = \sum_{k=1}^n f_k p_k(R) \quad (6)$$

When using Gaussians, the components are given by

$$p_k(R) = \frac{1}{\sqrt{2\pi\sigma_{rk}^2}} \exp\left\{-\frac{(R - r_{ok})^2}{2\sigma_{rk}^2}\right\}. \quad (7)$$

However, non-Gaussian basis functions may also be used (Hustedt et al., 2018). For a given model, the best-fit values of each of the parameters are those that minimize the reduced χ^2 value:

$$\chi_v^2 = \frac{1}{(N - q)} \sum_{i=1}^N \frac{[V_i - O_i B_i]^2}{\sigma^2}, \quad (8)$$

where V_i is the experimentally measured signal at the i th time point, O_i and B_i are the calculated intramolecular and background signals, σ^2 is the estimated noise variance, N is the total number of data points, and q is the total number of parameters considered in the fit. The use of a mathematical model to define $P(R)$, specifically the use of a Gaussian basis set, was originally used by Spiess and coworkers (Pannier et al., 2000a), then by Fajer and coworkers (Sen et al., 2007), and has been further developed by us (Brandon et al., 2012; Stein et al., 2015; Hustedt et al., 2018).

Previously, we introduced the Akaike information criterion corrected for finite sample size (AICc; Stein et al., 2015) and the Bayesian information criterion (BIC; Hustedt et al., 2018) for selecting an optimal model from a set used to analyze single

DEER datasets based on the principle of parsimony. The set of models considered can test different n values, different basis functions, or differing background decay functions.

$$AICc = N \ln \left[\frac{\sum_{i=1}^N (V_i - O_i B_i)^2}{N} \right] + 2(q+1) \left(1 + \frac{q+2}{N-q-2} \right) \quad (9)$$

$$BIC = N \ln \left[\frac{\sum_{i=1}^N (V_i - O_i B_i)^2}{N} \right] + (q+1) \ln N \quad (10)$$

These criteria balance the decrease in the sum of squared residuals (SSR) [$SSR = \sum_{i=1}^N (V_i - O_i B_i)^2$] versus the increase in the number of free parameters, q , that comes with increasing model complexity. When selecting from a group of models that have been tested, that with the lowest criterion value can be considered to be the optimal balance of these two factors (Burnham and Anderson, 2002). In practice, we find that the use of BIC is favored over AICc because the former favors more parsimonious models.

The magnitude of the BIC values do not directly reflect the merit of a particular model and cannot be used to determine that a particular model is correct. Their relative values are, however, significant. Setting BIC_0 equal to the lowest BIC value of the set, different models can be compared by calculating ΔBIC values.

$$\Delta BIC = BIC - BIC_0 \quad (11)$$

These ΔBIC values do reflect the relative merit of different models. Rules of thumb have been developed for interpreting ΔBIC values (Raftery, 1995; Burnham and Anderson, 2002). If the ΔBIC value for a particular model from a set under consideration is >10 , then the evidence against that model is very strong, and if <2 , it is weak. The use of BIC over AICc or any other criterion for model selection is subjective. Additional considerations, if properly justified, can be used to select an appropriate model.

Other approaches to the analysis of DEER data include the commonly used Tikhonov regularization (Chiang et al., 2005; Jeschke et al., 2006; Ibáñez and Jeschke, 2020; Ibáñez et al., 2020), alternative regularization approaches (Ibáñez and Jeschke, 2019), denoising methods followed by singular value decomposition (Srivastava and Freed, 2017; Srivastava et al., 2017; Srivastava and Freed, 2019), and neural networks (Worswick et al., 2018; Amey et al., 2021).

Model-based analysis of DEER data

The model-based approach to the analysis of DEER data is illustrated in Fig. 2 using data from T4 lysozyme (T4L) labeled at residues 65 and 80 with the methanethiosulfonate spin label (MTSSL). After a trivial scaling and shift of the time axis, the DEER data are fit using a model-based approach that includes the best-fit background factor. The optimal fit, according to BIC values, models $P(R)$ as a sum of two Gaussians. Table 1 gives the statistics obtained from fitting the data in Fig. 2 to $n = 1, 2$, and 3 Gaussian components. The BIC values for the $n = 1$ and $n = 3$ models both differ from that of the $n = 2$ model by <10 , suggesting that none of these models can be strongly rejected based on this dataset. In fact, the $n = 3$ model is preferred

according to the AICc values. The small amplitude of the third component and the large uncertainty of this amplitude (0.02 ± 0.06), together with the very narrow width of this Gaussian (0.04 ± 2.81 Å), all support the rejection of this more complex model (see Table 2).

The second component in the optimal $P(R)$ does not give rise to a distinct second mode and is fully consistent with a single backbone conformation of T4L with some inherent disorder and a distribution of rotameric states of the two labels. In other cases discussed below, individual well-separated Gaussian components clearly correspond to distinct backbone conformations. A general rule of thumb is that the number of conformations is less than or equal to the number of Gaussian components.

As has been previously discussed (Hustedt et al., 2018), model-based analysis allows for rigorous error analysis of the best-fit parameter values and the calculation of a confidence band for the best-fit distance distribution from the full covariance matrix using propagation of errors. The 2σ (95%) confidence band for the best-fit $n = 2$ Gaussian $P(R)$ is shown in Fig. 2 C as a shaded region and reproduced in Fig. 2 D along with the best-fit $P(R)$ for 15 replicate datasets collected for the same sample. These results demonstrate that the confidence band obtained from fitting a given dataset properly estimates the reproducibility of the distance distribution.

The $P(R)$ obtained using Tikhonov regularization is also shown in Fig. 2 C. The model-free $P(R)$ is quite close to the $P(R)$ modeled as the sum of two Gaussians. Both the model-based approach as developed primarily at Vanderbilt University (Brandon et al., 2012; Stein et al., 2015; Hustedt et al., 2018) and the model-free approach using Tikhonov regularization, as developed primarily by Jeschke et al. (2006), have been extensively used to analyze DEER data and are well documented. Although historically the use of Tikhonov regularization to give model-free fits to DEER data has required an initial background correction step, recently an approach for applying Tikhonov regularization to uncorrected data has been developed (Ibáñez and Jeschke, 2020; Ibáñez et al., 2020).

Videos demonstrating the use of either DD (Video 1) or GLADDvu (Video 2) to perform the model-based fits of this T4L dataset are available online. DD and GLADDvu are available for download at <https://github.com/erichustedt/>.

Global analysis paradigm

A set of DEER experiments collected under different experimental conditions can contain information far beyond what can be inferred from the collection of $P(R)$ obtained from individual fits to the traces. In Fig. 1 B, each conformation leads to an interlabel distance distribution that can be modeled as a single Gaussian component whose width is determined by the distribution of rotameric states of the labels. In practice, conditions may not be available that would allow the collection of data corresponding to the pure OO or OC conformations. Instead, different conditions, here ligand bound and ligand free (apo), favor the OC and OO conformations, respectively (Fig. 3 A). Qualitatively, the data and the $P(R)$ are consistent with a shift in the equilibrium from one favoring OO to OC upon ligand binding.

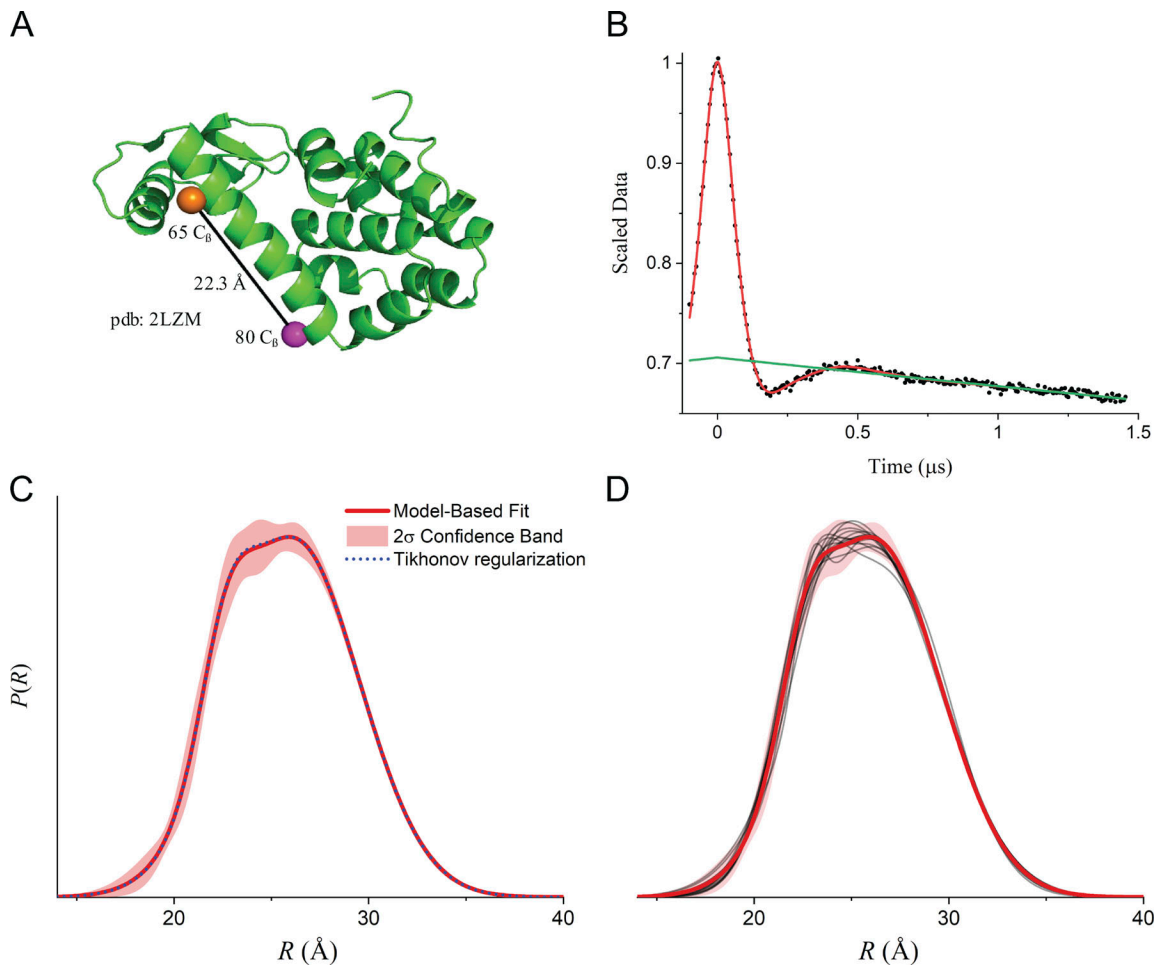


Figure 2. **Q-band DEER data and fit for T4L spin-labeled with MTSSL at residues 65 and 80.** (A) The crystal structure of T4L (PDB accession no. 2LZM; Matsumura et al., 1989) showing the location of the two spin labels. pdb, Protein Data Bank. (B) The scaled DEER data are shown as filled black circles together with the best model-based fit (red line) and background factor (green line). (C) The best-fit $P(R)$ modeled as the sum of two Gaussians is shown as a red line with the associated 2σ (95%) confidence band as a shaded region. The model-free $P(R)$ obtained using Tikhonov regularization in DeerAnalysis 2019 is also shown (dotted blue line). The optimal regularization factor was determined by generalized cross-validation and the starting time point for background fitting using the validation tool. (D) The solid red line and shaded region duplicate those shown in C. The best-fit $P(R)$ modeled as the sum of 2 Gaussians obtained from 15 replicate datasets are shown as thin black lines.

$$\begin{aligned} P_{apo}(R) &= (1 - C_{OO}^{apo})P'_{OC}(R) + C_{OO}^{apo}P'_{OO}(R) \\ P_{ligand}(R) &= (1 - C_{OO}^{ligand})P'_{OC}(R) + C_{OO}^{ligand}P'_{OO}(R) \end{aligned} \quad (12)$$

where C_{OO}^{apo} and C_{OO}^{ligand} are the fractions of apo and ligand-bound transporter in the OO state. Likewise, $P'_{OC}(R)$ and $P'_{OO}(R)$ are the interspin distance distributions of the pure OC and OO states.

More generally, the $P(R)$ for condition i can be expressed as a common set of $P'(R)$ corresponding to M different conformations.

$$P_i(R) = \sum_{j=1}^M C_j^i P'_j(R) \quad (13)$$

A more pertinent analysis of the data in Fig. 3 B would allow one to recover estimates of the distance distributions, $P'(R)$, for structural modeling of the pure conformational states and the set of coefficients, C , for defining equilibrium constants and other thermodynamic parameters. This tutorial focuses on the linked fitting of the datasets (i.e., the global analysis of multiple

Table 1. **Model statistics from fitting of T4L 65/80 data in Fig. 2**

n	q	SSR	χ^2_u	AICc	BIC	$\Delta AICc$	ΔBIC
1	5	0.001984	1.0803	-3,051.3	-3,030.3	17.5	5.4
2	8	0.001823	1.0042	-3,067.0	-3,035.7	1.8	0
3	11	0.001765	0.9842	-3,068.8	-3,027.3	0	8.3

Table 2. Fit parameters for T4L 65/80 data in Fig. 2

<i>n</i>	1	2	3
Δ	0.298 ± 0.002	0.297 ± 0.002	0.30 ± 0.02
η	4.61 ± 0.01	4.61 ± 0.01	4.61 ± 0.01
Scale	1.003 ± 0.002	1.001 ± 0.002	1.00 ± 0.03
r_0	25.73 ± 0.06	22.8 ± 0.5	29 ± 4
σ_R	3.55 ± 0.08	1.3 ± 0.8	0.04 ± 2.81
Fraction		0.10 ± 0.09	0.02 ± 0.06
r_0		26.2 ± 0.4	26.1 ± 0.6
σ_R		3.4 ± 0.2	3.5 ± 0.2
Fraction		0.90 ± 0.09	0.86 ± 0.16
r_0			23.1 ± 0.7
σ_R			1.6 ± 1.0
Fraction			0.12 ± 0.16

DEER time traces) to obtain this full description of the system under investigation using models that explicitly link the conformations under different conditions.

To demonstrate putting these concepts into practice, consider the three simulated DEER traces in Fig. 4 that were calculated for bimodal $P(R)$ generated from the same two unimodal distributions selected from the test set generated by Edwards and Stoll (2018) with different relative amplitudes (Table 3). The underlying biological model is that the protein is undergoing a ligand-dependent shift in the equilibrium between two conformational states. Given the $P(R)$ obtained from fitting these data individually, either to bimodal Gaussian distributions (Fig. 4 B) or using a Tikhonov regularization (Fig. 4 C), it would be hard to argue convincingly whether the protein is or is not behaving according to this model of its functional dynamics (i.e., that the protein adopts the same two conformational states at all ligand concentrations albeit in different proportions).

However, when the fit requires the means and SDs of the two Gaussian components to be equal at different ligand concentrations, the best-fit distance distributions (Fig. 4 D) more accurately and precisely correspond to the true distributions. For this analysis, the background factors, η , the modulation depths, Δ , and the relative amplitudes of the two components vary for the three datasets (see Figs. S1, S2, and S3). The benefits of the linked global analysis are clearly demonstrated by considering the low-amplitude components in datasets A and C, which are poorly recovered in the individual fits, regardless of the approach used (Fig. 4, B and C). In the global fit, however, the same two Gaussian components are used to fit all three datasets. Both of the recovered Gaussians, shown as cyan lines in Fig. 4 E, agree well with the true components. Due to the ill-conditioned nature of the problem, the considerable differences between the best-fit distributions for the individual versus global fits (cf. Fig. 4, B and D) result in negligible changes in the best-fit DEER traces (cf. solid black and dashed colored lines in Fig. 4 A). Global analysis not only results in a more accurate recovery of the true distance distributions but also results in increased precision. This is

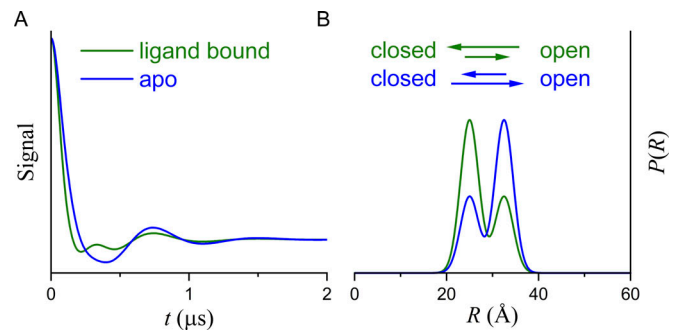


Figure 3. DEER data assuming that two conformations are in equilibrium. (A) Simulated DEER data assuming that ligand binding (green line) favors the OC state. (B) The corresponding $P(R)$.

reflected in the narrow confidence bands of the linked versus individual fits and in smaller parameter uncertainties (Table 3).

The global reduced χ^2 value is given by

$$\chi_v^2 = \frac{1}{(\sum_j N_j) - Q} \sum_{j=1}^M \sum_{i=1}^{N_j} \frac{[V_{ji} - (OB)_{ji}]^2}{\sigma_j^2}, \quad (14)$$

where Q is the total number of unique fit parameter values that are varied. As with fitting single datasets, BIC values can be used to select the optimal from a set of models used to fit multiple datasets. Eqs. 9 and 10 for AICc and BIC, respectively, both assume that the variance of the data is constant for all data points. Although this assumption is valid for DEER data from a single experiment that has not been background corrected, data from different experiments that are being globally analyzed will have different noise levels. Cavanaugh and Neath (1999) have shown that the derivation of the BIC does not require the assumption that the noise is identically distributed for all data points. Following Banks and Joyner (2017), we assume that each point in a given DEER dataset, j , has a variance $\sigma_j^2 = w_j^2 \sigma^2$ to give

$$\text{BIC}_{\text{WLS}} = N_{\text{Total}} \ln \left\{ \frac{\sum_{j=1}^M \sum_{i=1}^{N_j} \frac{[V_{ji} - (OB)_{ji}]^2}{w_j^2}}{N_{\text{Total}}} \right\} + (Q + 1) \ln N_{\text{Total}} \quad (15)$$

where $N_{\text{Total}} = \sum N_j$ is the total number of data points in the global analysis and Q is the total number of unique fit parameter values that are varied.

Table 4 shows the statistics obtained from fitting the three simulated datasets in Fig. 4 using six different models. Models 2, 4, and 6 use $n = 1, 2$, and 3 Gaussian components, each corresponding to a separate conformation with no parameters linked. Thus, these models are equivalent to fitting the data individually. For models 1, 3, and 5, all of the r_{0j} and σ_{Rj} values are linked, and the same set of Gaussian components is used to fit both datasets. Although the most complex model, 6, with $Q = 33$ gives the lowest SSR and χ_v^2 values, model 3 with $Q = 16$ gives the lowest BIC values and is strongly preferred.

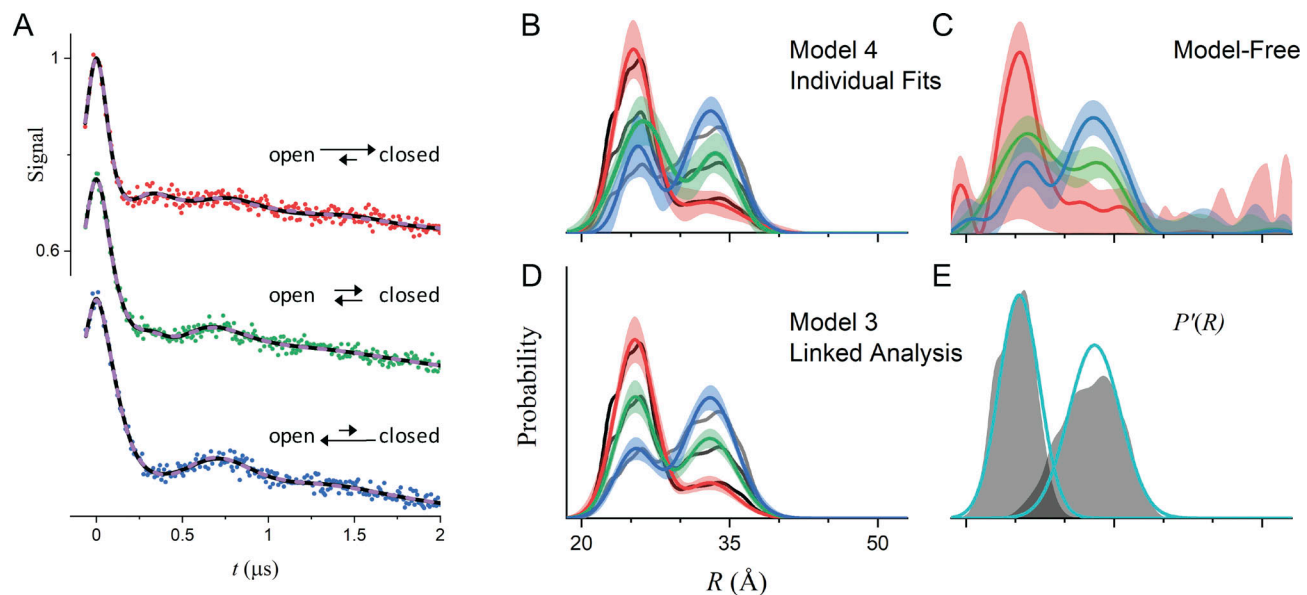


Figure 4. Global analysis of simulated DEER data. (A) The data (filled circles) were simulated for $P(R)$ modeled as the sum of two components using the amplitudes in Table 3. The true $P'(R)$ of the components are distributions 5347 and 483 from the set of distributions calculated by Edwards and Stoll (2018) using MMM (Jeschke, 2018b) for T4L labeled at 118/154 and 8/126 with means/SDs of 25.1/1.9 Å and 32.6/3.0 Å, respectively. The best-fit lines for model 3 (R_0 and σ_R values linked) and model 4 (no parameters linked) are shown as solid black and dashed colored lines, respectively. (B) $P(R)$ for model 4 for datasets A (red), B (green), and C (blue) with the associated 2σ (95%) confidence bands as shaded regions. The black lines are the true $P(R)$ used for the simulations. (C) Best-fit $P(R)$ from Tikhonov regularization using DeerLab version 0.13.2 using the same color scheme. The optimal regularization factor was determined by generalized cross-validation. (D) Best-fit $P(R)$ for model 3 using the same color scheme with the associated 2σ (95%) confidence bands as the shaded regions. The black lines are the true $P(R)$ used for the simulations. (E) The $P'(R)$ obtained for model 3 is shown in cyan, and the true $P'(R)$ used for the simulations is superimposed as shaded regions. Both the x and y axis scales are the same for B–E.

A core principle of global analysis is that the models tested should move beyond mathematical statements about the functions and parameter sets used to fit data and incorporate the fundamental biological questions being addressed in the experiments (Beechem et al., 1991; Beechem, 1992). Moving beyond loose interpretations of the peaks in the $P(R)$ obtained from individual fits, the results in Fig. 4 and Table 4 allow a DEER practitioner to confidently assert that the data are consistent with, and in fact optimally modeled, as a protein undergoing a ligand-dependent shift in the equilibrium between two conformational states that are themselves ligand independent.

With the recent development of the DeerLab software package (Ibáñez et al., 2020), it is now possible to perform a global analysis of DEER data using Tikhonov regularization. The results of such an analysis of these three simulated datasets are shown

in Fig. S4. Note that unlike model-based fitting (Fig. 4 E), the regularization-based global analysis (Fig. S4 C) does not correctly disentangle the two component distributions corresponding to the two conformations in equilibrium. In this tutorial, we focus on the use of our GLADDvu software for the model-based global analysis of DEER data.

A description of how parameters are linked in GLADDvu is provided in the Appendix. Screenshots showing the use of GLADDvu to fit these simulated datasets to model 3 are shown in Figs. S1, S2, S3, S5, and S6. A demonstration of the use of GLADDvu to perform all of the fits listed in Table 4 is available in Video 3.

Global analysis of DEER data

Global analysis has long been used to fit both linear and saturation transfer EPR continuous wave EPR data to determine

Table 3. Fit parameters for simulated data in Fig. 4

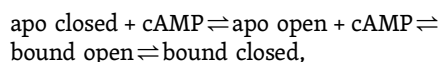
Data set		A		B		C	
Simulation	Fraction	0.75	0.25	0.5	0.5	0.25	0.75
Fit to model 3: linked analysis	r_0	25.4 ± 0.3	33.0 ± 0.4	25.4 ± 0.3	33.0 ± 0.4	25.4 ± 0.3	33.0 ± 0.4
	σ_r	2.0 ± 0.3	2.6 ± 0.4	2.0 ± 0.3	2.6 ± 0.4	2.0 ± 0.3	2.6 ± 0.4
	Fraction		0.20 ± 0.04		0.46 ± 0.05		0.70 ± 0.06
Fit to model 4: individual fits	r_0	25.2 ± 0.4	32.8 ± 3.1	26.2 ± 0.9	33.7 ± 1.1	25.6 ± 0.7	33.1 ± 0.5
	σ_r	1.9 ± 0.4	3.4 ± 2.6	2.6 ± 0.9	2.1 ± 0.9	1.6 ± 0.7	2.6 ± 0.5
	Fraction		0.24 ± 0.15		0.36 ± 0.14		0.70 ± 0.07

Table 4. Model statistics from fitting simulated data in Fig. 4

Model	<i>n</i>	Linked	<i>q</i>	SSR	χ^2_0	BIC	Δ BIC
1	1	r_0 and σ_r	11	0.13044	1.7759	-6776.0	422.3
2	1	Nothing	15	0.08557	1.1268	-7106.9	91.4
3	2	r_0 and σ_r	16	0.07588	0.9945	-7198.3	0.0
4	2	Nothing	24	0.07503	0.9945	-7153.3	45.1
5	3	r_0 and σ_r	21	0.07532	0.9944	-7170.2	28.1
6	3	Nothing	33	0.07377	0.9878	-7108.0	90.3

The models differ in the number of Gaussian components, *n*, used to define the distance distributions and in how their parameters are linked for the different datasets. In all models, the modulation depths, Δ , and the background parameters, η , for the different datasets are not linked. A video (Video 3) demonstrating the use of GLADDvu to perform the fits of these simulated data is available.

parameters defining either the global rotational diffusion (Hustedt et al., 1993; Hustedt and Beth, 1995, 2001; Stein et al., 2002; Hustedt and Beth, 2004) or the distance between and relative orientation (Hustedt and Beth, 1996; Hustedt et al., 1997; Hustedt and Beth, 1999; Ghimire et al., 2012; Sahu et al., 2014) of spin labels. In an early example of the use of global analysis for DEER data, Goldfarb and colleagues investigated the cAMP-induced conformational change in the carboxy-terminal cyclic nucleotide binding domain (NBD) of the HCN2 ion channel (Collauto et al., 2017). A total of 26 DEER datasets collected either at equilibrium as a function of cAMP concentration or at varying time points following addition of stoichiometric cAMP using a microfluidic rapid freeze quench apparatus. All datasets were fit with three Gaussian components representing two different conformations: open and closed. The centers and widths of the three Gaussians and the relative amplitude of the two Gaussian components representing the open state were linked. The relative fractions of the open versus closed states were varied across the different datasets. Modeling the ligand-induced conformational transition using a four-state model,



the fractions of the open and closed conformations were used to quantify the three corresponding equilibrium constants and to estimate the six transition rates.

Mchaourab and coworkers have globally analyzed DEER data to investigate the ligand-dependent functional dynamics of a number of membrane transporters, including ion-dependent secondary transporters (Masureel et al., 2014; Dastvan et al., 2016; Martens et al., 2016; Claxton et al., 2018; Paz et al., 2018; Jagessar et al., 2020) and ATP-dependent multidrug transporters (Mishra et al., 2014; Verhalen et al., 2017; Dastvan et al., 2019). Using previously published data, we present below details of how global analysis has advanced the understanding of ligand-dependent conformational equilibrium in a way that would not be possible from the individual fits.

P-glycoprotein 1 (Pgp)

The use of DEER to investigate the conformational dynamics of the ABC transporter Pgp provides an instructive example of the benefits of global analysis. Although the initial DEER study was

performed on the basis of a single crystal structure (Verhalen et al., 2017), the recent determination of multiple cryo-EM structures (Alam et al., 2018; Kim and Chen, 2018; Alam et al., 2019) illustrates the unique and complementary insight contributed by DEER analysis (Dastvan et al., 2019). Pgp is a mammalian ATP-binding cassette transporter capable of pumping a wide array of xenobiotic substrates out of cells (Aller et al., 2009; Jin et al., 2012; Li et al., 2014; Kim and Chen, 2018). Moreover, a number of inhibitors have been developed in search of a strategy to increase the efficacy of cancer chemotherapy (Chufan et al., 2016). Here, we focus on data collected in the presence of different substrates and inhibitors of Pgp.

An extensive set of spin label pairs was introduced to study the functional dynamics of Pgp under different biochemical conditions that favor specific conformational states (Verhalen et al., 2017; Dastvan et al., 2019). Here, we focus on a pair of sites, 511 and 1043, within NBDs 1 and 2, respectively, which come together to form two nucleotide binding sites (NBS; Fig. 5). In the presence of ATP and inorganic vanadate (V_i), Pgp can form a state that mimics the post-hydrolysis transition state where ADP and phosphate are trapped in the binding sites. Under these conditions, DEER data from Pgp show an equilibrium between distinctly different conformational states (Verhalen et al., 2017) dependent on the substrate present. Fig. 6 shows 10 DEER traces collected for Pgp labeled at 511/1043 in the presence of ATP/ V_i and either no substrate, 7 different substrates, or 2 inhibitors of transport (Dastvan et al., 2019).

The analysis of these 10 datasets individually using either Tikhonov regularization or model-based fitting gives broad multicomponent distance distributions that depend strongly on the substrate (Fig. S7). Using either approach, however, it is difficult to draw firm conclusions about the conformations evident in these distributions. To test the utility of global analysis for these data, three different models were used in combined fits (Table 5). Models 1 and 2 employ three and four conformational states, respectively, each modeled as a single Gaussian component. The r_0 and σ_r values of these Gaussians were linked across all 10 datasets while the amplitudes of the components, the modulation depths, background factors, and scale factors varied. For the conformation with the shortest mean interspin distance, the two NBDs are tightly bound together, trapping ADP/ V_i within NBS 2. The intermediate distance component (and its

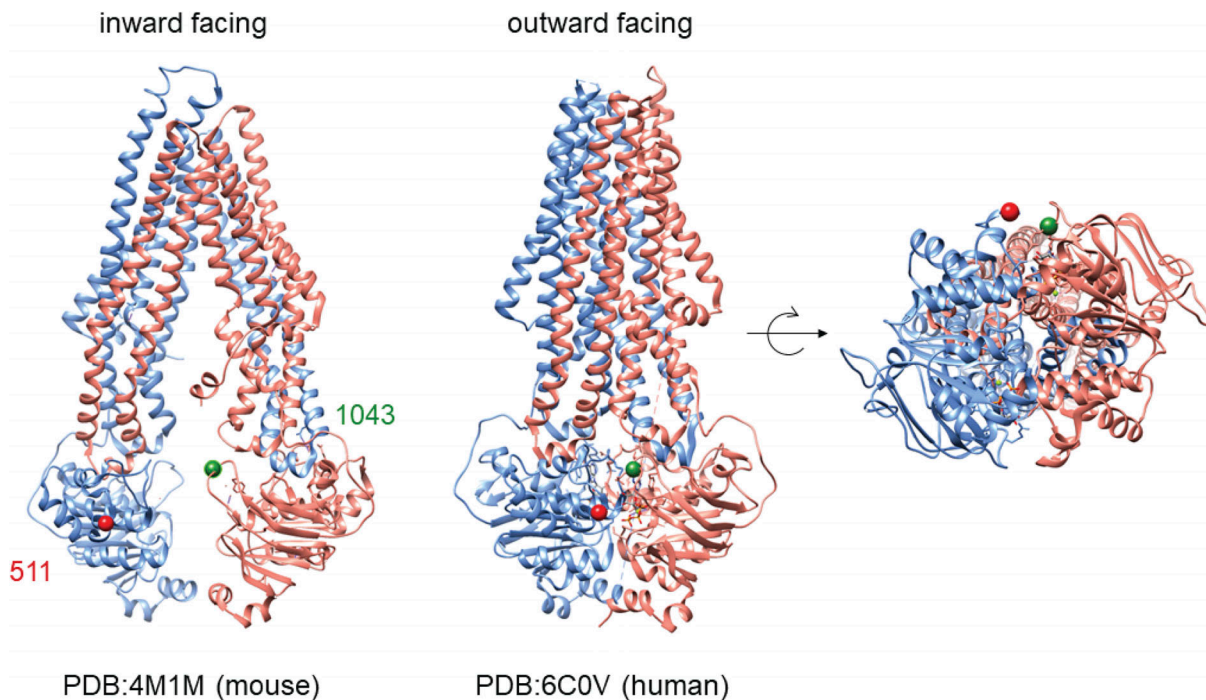


Figure 5. **The conformational shift of Pgp.** Left: The mouse Pgp structure in the inward-facing conformation (Li et al., 2014). Highlighted are two residues, 511 and 1043, which are on opposite halves of Pgp. Middle: The structure of human Pgp in the outward-facing conformation (Kim and Chen, 2018). Right: The closure of the NBDs is shown in detail, highlighting the nearness of the residues 511 and 1043 in the outward-facing conformation. PDB, Protein Data Bank.

corresponding conformation) is highly populated only in the presence of the two inhibitors, tariquidar and zosuquidar, or vinblastine, which can act as an inhibitor at high concentrations. The two components with the longest mean distances correspond to those seen in the absence of any nucleotide (apo state). Model 3 specifically tests whether the apo-like contributions to $P(R)$, evident at the longer distances, can be fit as a single conformation modeled by two Gaussian components with a linked ratio across all conditions. Based on the ΔBIC values in Table 5, model 2 is the optimal model. The increase in BIC ($\Delta\text{BIC} = 19.3$) for model 3 versus model 2 indicates that there are distinct apo-like conformations for different substrates. The separation of these underlying conformational states is much clearer using model-based global analysis, and the quality of the fits in Fig. 6 A suggests that, indeed, there is a common set of protein conformations across all 10 experimental conditions.

Global analysis also allows enhanced quantitative analysis of the relative populations of the various conformations. Those substrates that induced the largest population of the tightly bound component were most efficient in stimulating ATP turnover, resulting in a linear relationship between this component's population and the natural logarithm of stimulated ATP turnover rate constant, k_{cat} (Fig. 6 C; Dastvan et al., 2019). These results demonstrate that, using global analysis, the equilibrium populations of protein conformations determined from the global analysis of DEER data can be quantitatively related to the function dynamics of the protein and that important mechanistic insights can be obtained.

A demonstration of the use of GLADDvu to perform the fits of these Pgp datasets to models 1–3 is available in Video 4.

LmrP

LmrP is a multidrug transporter from *Lactococcus lactis* and a member of the major facilitator superfamily whose transport is driven by the proton gradient (Fig. 7; van Veen et al., 1999; van Veen, 2001). In a series of papers, DEER spectroscopy has been used to define the protonation-dependent isomerization of the transporter between inward-facing and outward-facing conformations (Masureel et al., 2014; Martens et al., 2016; Debruycker et al., 2020). Fig. 8 shows DEER data from LmrP collected at eight different pH values with labels placed at residues L160C and I310C at the extracellular ends of TM helices 5 and 10, respectively. In Fig. S8, the individual DEER traces have been analyzed using both model-based and model-free approaches. Collectively, these data are qualitatively consistent with a model where TM helices 5 and 10 move closer and become more ordered, closing the extracellular gate, as residues within the pore are protonated. The shift from the OO to OC state is reflected in a transition from a broad unimodal $P(R)$ at pH 8.0 centered at ~ 46 Å to a multimodal $P(R)$ at pH 4.6 with a narrower component centered at ~ 37 Å. This qualitative interpretation of these data raises the question of whether they are consistent with a single set of conformations of the protein, OO and OC, which would give rise to an ideal pair of distributions, $P'_{\text{oo}}(R)$ and $P'_{\text{oc}}(R)$, respectively. If so, for each of the $P_i(R)$ corresponding to the eight datasets

$$P_i(R) = [1 - C_{\text{oo}}(\text{pH})]P'_{\text{oc}}(R) + C_{\text{oo}}(\text{pH})P'_{\text{oo}}(R),$$

where $C_{\text{oo}}(\text{pH})$ is the pH-dependent fraction of the protein in the OO conformation. $P'_{\text{oo}}(R)$ and $P'_{\text{oc}}(R)$ can be used for modeling the two conformational states of the protein, and the set of $C_{\text{oo}}(\text{pH})$

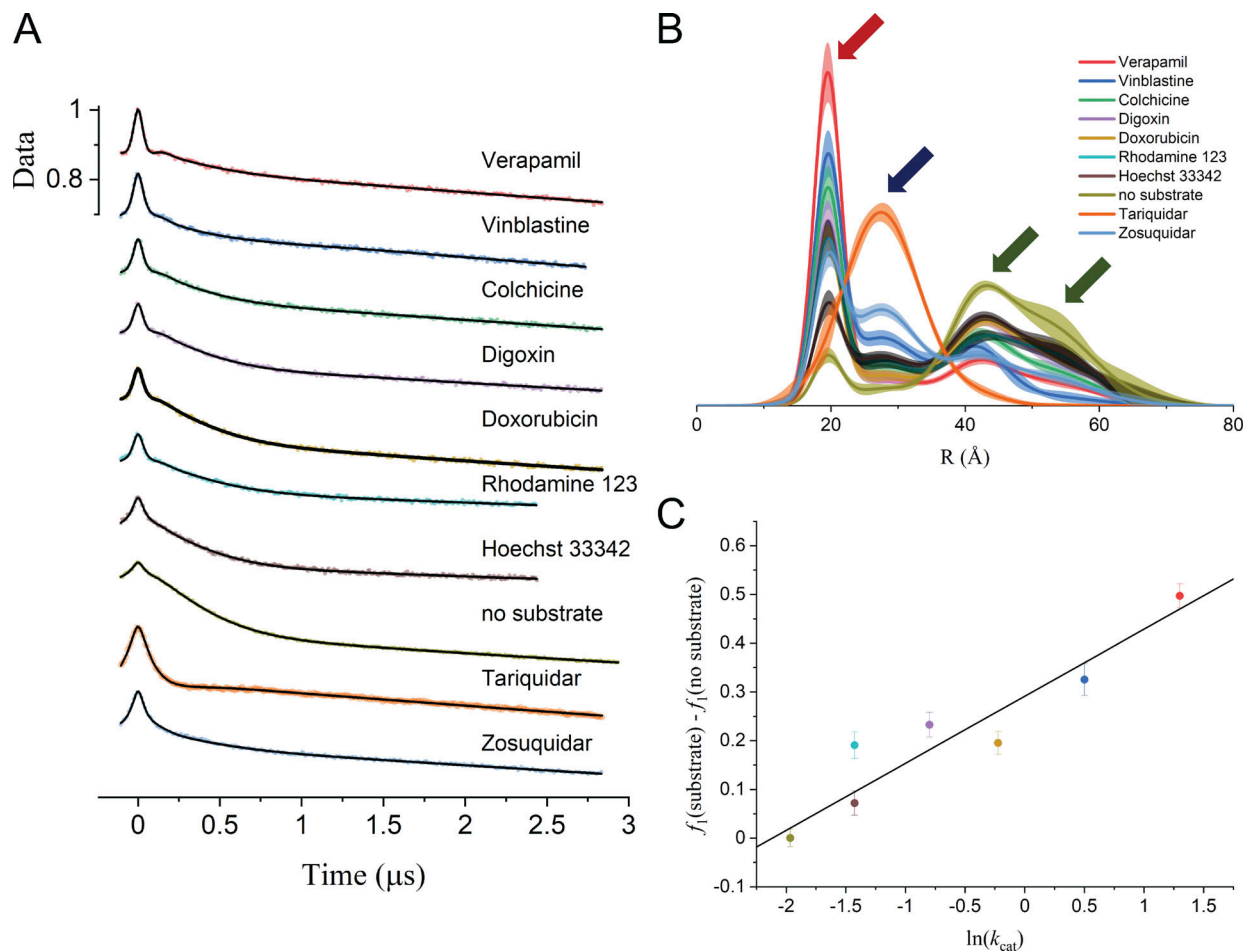


Figure 6. **Global analysis of Q-band DEER data for Pgp spin labeled with MTSSL at residues 511 and 1043.** (A) Samples were prepared in mixed micelles with ATP and V_i in the presence and absence of substrates and inhibitors as indicated (Dastvan et al., 2019). The scaled data are shown as filled colored circles, and the best fits obtained from global analysis using model 2 (Table 5) are shown as solid black lines. (B) The best-distance distributions obtained using model 2 to fit the Pgp data with the associated 2σ (95%) confidence bands as shaded regions. The R_0 values of the four components are indicated by the arrows. (C) The substrate-induced population of the shortest distance component is correlated with the activation energy of ATP turnover.

can be used for quantifying the equilibrium between the two conformations, providing a measure of the pH dependence of the stability of the two conformations.

Using the model-based approach, all of the DEER traces with the exception of the pH 6.0 data are optimally fit with $n = 2$ Gaussian components. At the lower pH values, the two components with means separated by ~ 10 Å clearly correspond to OC and OO conformations. At the higher pH values, the two

components have similar r_0 values, one broad and one narrow. These results suggest that three Gaussian components will be needed for the optimal global fit to the eight traces and raise the question of what the broad component evident at higher pH values represents.

The full set of models tested against the eight LmrP DEER traces are listed in Table 6. Models 1 and 2 fit the datasets individually with two or three Gaussian components and no

Table 5. **Statistics of fitting Pgp data (Fig. 6)**

Model	n	Linked	q	SSR	χ^2_v	BIC _{WLS}	Δ BIC _{WLS}
1	3	Gaussians	56	2.5980E-02	1.2183	-36,842.8	62.2
2	4	Gaussians	68	2.4681E-02	1.1593	-36,905.0	0.0
3	4	Gaussians and ratio of two longest	59	2.5623E-02	1.1921	-36,885.7	19.3

The models differ in the number of Gaussian components, n , used to define the distance distributions and in how their parameters are linked for the different datasets. In all models, the modulation depths, Δ , and the background parameters, η , for the different datasets are not linked. A video (Video 4) demonstrating the use of GLADDvu to perform the fits of these Pgp data is available.

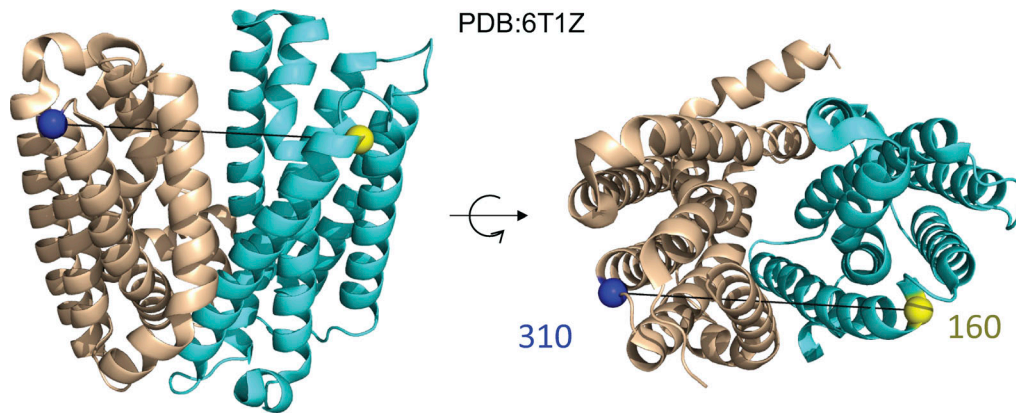


Figure 7. **X-ray crystal structure of LmrP.** Related to [Debruycker et al. \(2020\)](#). On the left is a side view of LmrP, and on the right is the top (extracellular) view of LmrP. Highlighted are two residues, 160 and 310, on opposite halves of LmrP where spin labels have been placed. PDB, Protein Data Bank.

parameters linked. Models 3 and 4 fit the data globally with two or three conformations, with each modeled as a single Gaussian component. For these models, the values of r_0 and σ_r are linked across all datasets, and the amplitudes, modulation depths, backgrounds, and scale factors are not linked. Models 5, 6, and 7 all use three Gaussians with the values of r_0 and σ_r linked and different ways of linking some of the amplitude variables. For model 5, the OC conformation is modeled by a single Gaussian, and the OO conformation is modeled by two Gaussians, with a linked ratio across all eight traces. For model 6, the OO conformation is modeled by a single Gaussian, and the OC conformation is modeled by two Gaussians, with a linked ratio across all eight traces. For model 7, the OO and OC conformations are both modeled by single Gaussians, and a third component contributes a linked fraction across all eight datasets.

Of the seven models tested, model 7 is optimal according to the BIC values (Table 6). Model 7 fits the data to $n = 3$ Gaussian components (Fig. 8). For two of these, the fractional contribution is pH dependent, one corresponding to OC state ($r_0 = 36.5 \pm 0.1 \text{ \AA}$; $\sigma_r = 0.8 \pm 0.1 \text{ \AA}$) and one corresponding to the OO state ($r_0 = 47.4 \pm 0.1 \text{ \AA}$; $\sigma_r = 2.1 \pm 0.4 \text{ \AA}$). The fractional contribution of the third Gaussian ($r_0 = 42.4 \pm 4.8 \text{ \AA}$; $\sigma_r = 5.0 \pm 1.7 \text{ \AA}$) is independent of pH. This third component could account for one or more of a number of factors, including non-Gaussian character of the true $P(R)$, deviation of the background factors from true exponentials, or the presence of nonfunctional protein in the sample. Assuming the latter, the fraction of OO functional protein have been plotted and fit to determine a pK for the transition between the two conformations. Significantly, when the appropriate values of $C_{oo}(\text{pH})$ are fit to a titration curve, models 3, 5, 6, and 7 all give similar pK values (Table 6). Although including a third, pH-independent population did not affect the pK determined from the titration, the ability to identify such nonfunctional proteins can in future studies spur changes and optimization of purification protocols.

Looking ahead

GLADDvu was designed to be a fully flexible tool suitable for a wide variety of experimental situations beyond the examples

presented in this tutorial. These examples demonstrated how global analysis of DEER data from one spin-labeled mutant obtained under different ligand conditions gives enhanced qualitative insights into the functionally relevant dynamics of integral membrane proteins complete with error analysis of the fit parameters. One could consider analyzing data from multiple mutants under a common set of ligand conditions with different $P'(R)$ and a common set of C_j^i . Such analyses would test whether domains are moving as rigid bodies or whether the spin labels have any influence on equilibrium coefficients.

The model-based approach available with GLADDvu allows the ligand-dependent fractions of various components to be determined by the fit while providing the uncertainties of the parameters as well as the confidence bands for the distance distributions. Recently, a model-free approach to the global analysis of DEER data has been developed ([Ibáñez and Jeschke, 2020](#); [Ibáñez et al., 2020](#)). As is the case for the analysis of individual time traces, different approaches to the global analysis of multiple datasets will provide complementary insights into the fundamental biological issues under investigation.

Online supplemental material

Fig. S1 shows a screenshot of the answer panel for dataset A of GLADDvu during the global analysis of simulated data using model 3. Fig. S2 shows a screenshot of the answer panel for dataset B of GLADDvu during the global analysis of simulated data using model 3. Fig. S3 shows a screenshot of the answer panel for dataset C of GLADDvu during the global analysis of simulated data using model 3. Fig. S4 shows a global analysis of the same simulated DEER data as in Fig. 4 using Tikhonov regularization. Fig. S5 shows a screenshot of the Fit panel of GLADDvu during the global analysis of simulated data using model 3. Fig. S6 shows a screenshot of the $P(R)$ panel of GLADDvu during the global analysis of simulated data using model 3. Fig. S7 shows distance distributions from individual fits to the DEER data for Pgp in Fig. 6. Fig. S8 shows results from individual fits for LmrP data in Fig. 8. Videos 1, 2, 3, and 4 demonstrate the fitting of the data in Fig. 2 using DD and the fitting of the data in Figs. 2, 4, and 6 using GLADDvu, respectively.

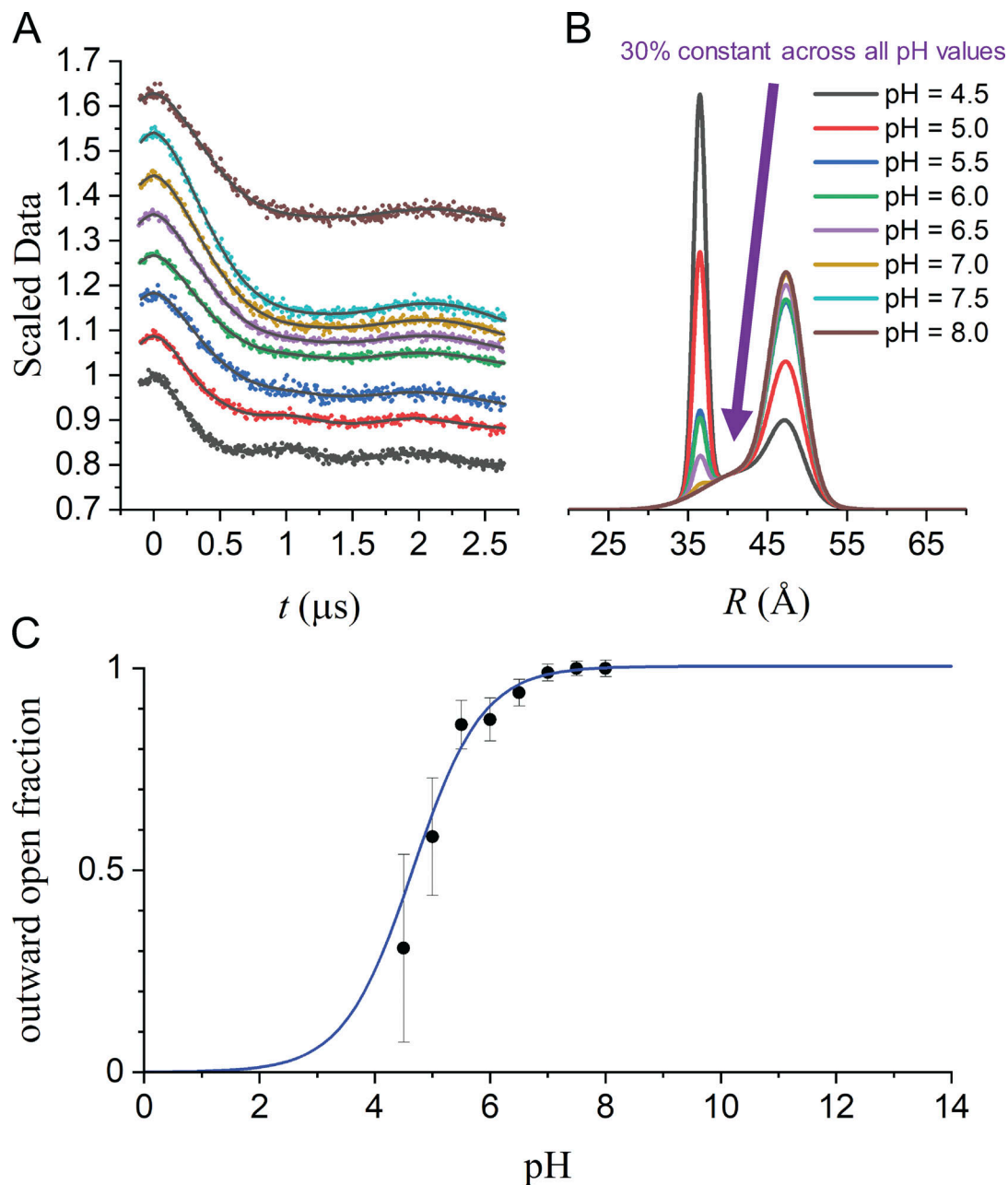


Figure 8. **Global analysis of Q-band DEER data for LmrP spin labeled with MTSSL at residues 160 and 310.** Related to Masureel et al. (2014). Samples were prepared in dodecyl maltoside micelles at eight different pH values ranging from 4.5 to 8.0 as indicated. **(A)** Overlay of all eight datasets and the fits obtained from global analysis using model 7 in Table 6. **(B)** The $P(R)$ obtained for model 7. **(C)** The OO fraction obtained for model 7 as a function of pH fit to determine the pK value.

Appendix GLADDvu

Our MATLAB software, DD, for the model-based fitting of single DEER datasets has been described in detail elsewhere (Brandon et al., 2012; Stein et al., 2015; Hustedt et al., 2018). A separate MATLAB program, GLADDvu, has been developed for globally fitting multiple DEER datasets. GLADDvu is designed for maximal flexibility, allowing the user to create both simple and complex models with parameters that are fixed, floated, or linked as desired. A fixed parameter is kept at its initial value and is not varied during the fit. A floated parameter is varied to

find the best-fit values that minimize the global reduced χ^2 value. A linked parameter for one experimental dataset is required to have the same value as another floated parameter for the same or a different dataset.

After reading in multiple files, each dataset is phased. Then, for each separate experiment, the 0 of the time axis is adjusted such that the signal maximum occurs at $t = 0$, and the values of the DEER signal are scaled such that $V(t = 0) \approx 1$. The noise variance for a given dataset, σ_m^2 , is estimated from the variance of its imaginary component. Various background models can be selected, including exponential, stretched exponential, and

Table 6. Models used to fit LmrP data (Fig. 8)

Model	<i>n</i>	Linked	<i>q</i>	SSR	χ^2_0	BIC _{WLS}	Δ BIC _{WLS}	pK
1	2	Nothing	64	0.075598	1.1230	−30,382.8	139.7	—
2	3	Nothing	88	0.074582	1.1129	−30,242.2	280.4	—
3	2	Gaussians	36	0.079455	1.1651	−30,474.8	47.7	4.6 ± 0.6
4	3	Gaussians	46	0.077139	1.1329	−30,483.0	39.6	—
5	3	Custom	39	0.078279	1.1463	−30,498.7	23.8	4.6 ± 0.7
6	3	Custom	39	0.078139	1.1419	−30,509.5	13.1	4.8 ± 1.0
7	3	Custom	39	0.077450	1.1365	−30,522.6	0.0	4.7 ± 1.3

The models differ in the number of Gaussian components, *n*, used to define the distance distributions and in how their parameters are linked for the different datasets. In all models, the modulation depths, Δ , and the background parameters, η , for the different datasets are not linked. pK values are the negative logarithms of the dissociation constants.

excluded volume. The distance distribution can be modeled as the sum of *n* components (Eq. 6), including Gaussians (Eq. 7). Minimization of χ^2_0 is attempted using MATLAB's interior point, global search, or particle swarm algorithms.

The model used to analyze data are specified by the Background, Components, Shape, and Linked dropdown menus and can be further modified using the individual Answer File spreadsheets for each dataset (Figs. S1, S2, and S3). As seen in the third column of these spreadsheets, for each of the three datasets, there are eight parameters that are floated (i.e., they are not fixed). These are Δ (depth), η (eta), r_{01} , σ_{r1} , r_{02} , σ_{r2} , a_2 (amp₂), and a scale factor (~ 1). The r_{01} , σ_{r1} , r_{02} , and σ_{r2} parameters for experiments 2 and 3 are linked to the corresponding parameters for experiment 1, as specified in the fourth and fifth columns of the Answer File spreadsheet, ensuring that the same two Gaussian components are used to define the best-fit *P*(*R*) for the two datasets.

The parameter dimension corresponds to *d* in Eq. 5. For *d* = 3, concentration is the effective spin concentration assuming a homogeneous 3-D solution of spins for the given modulation depth.

$$[spin] (\mu\text{M}) = 0.001 \times \frac{10^\eta}{\Delta}$$

The parameters β and ζ can be used for defining three non-Gaussian component shapes, a generalized normal distribution with nonzero excess kurtosis, a skew normal distribution with nonzero skew, and a generalized skew normal distribution with nonzero excess kurtosis and skew as defined in equations S1–S3 of Hustedt et al. (2018). Here, the parameters are automatically fixed to values, $\beta = 2$ and $\zeta = 0$, appropriate for Gaussian components.

The fits to the data and corresponding *P*(*R*) are displayed in the fit (Fig. S5) and *P*(*R*) (Fig. S6) panels, respectively. Statistics for all fits are displayed in the statistics panel. Videos are provided to demonstrate the use of DD and GLADDvu to perform the fits included in this tutorial.

Acknowledgments

Joseph A. Mindell served as editor.

This work was supported by National Institutes of Health grants GM128087 and GM077659 (H.S. Mchaourab). R.A. Stein

was also supported by National Institutes of Health grants GM113195 (M. Maduke), MH070039 (J.E. Gouaux), NS117873 (J. Cordero Morales), GM124310 (A. Rajca), and DC007664 (D. Minor).

The authors declare no competing financial interests.

Author contributions: All authors contributed to the conceptual development of this work. E.J. Hustedt and H.S. Mchaourab wrote the manuscript with the assistance of R.A. Stein. E.J. Hustedt wrote DD and GLADDvu with significant input from R.A. Stein. R.A. Stein provided all of the experimental data in collaboration with authors of the referenced papers.

Submitted: 23 December 2020

Accepted: 30 August 2021

References

- Ackermann, K., J.L. Wort, and B.E. Bode. 2021. Nanomolar pulse dipolar EPR spectroscopy in proteins: Cu^{II}-Cu^{II} and nitroxide-nitroxide cases. *J. Phys. Chem. B*. 125:5358–5364. <https://doi.org/10.1021/acs.jpcc.1c03666>
- Alam, A., R. Küng, J. Kowal, R.A. McLeod, N. Tremp, E.V. Broude, I.B. Roninson, H. Stahlberg, and K.P. Locher. 2018. Structure of a zosuquidar and UIC2-bound human-mouse chimeric ABCB1. *Proc. Natl. Acad. Sci. USA*. 115:E1973–E1982. <https://doi.org/10.1073/pnas.1717044115>
- Alam, A., J. Kowal, E. Broude, I. Roninson, and K.P. Locher. 2019. Structural insight into substrate and inhibitor discrimination by human P-glycoprotein. *Science*. 363:753–756. <https://doi.org/10.1126/science.aav7102>
- Alexander, N., M. Bortolus, A. Al-Mestarihi, H. Mchaourab, and J. Meiler. 2008. De novo high-resolution protein structure determination from sparse spin-labeling EPR data. *Structure*. 16:181–195. <https://doi.org/10.1016/j.str.2007.11.015>
- Alexander, N.S., R.A. Stein, H.A. Koteiche, K.W. Kaufmann, H.S. Mchaourab, and J. Meiler. 2013. RosettaEPR: rotamer library for spin label structure and dynamics. *PLoS One*. 8:e72851. <https://doi.org/10.1371/journal.pone.0072851>
- Aller, S.G., J. Yu, A. Ward, Y. Weng, S. Chittaboina, R. Zhuo, P.M. Harrell, Y.T. Trinh, Q. Zhang, I.L. Urbatsch, et al. 2009. Structure of P-glycoprotein reveals a molecular basis for poly-specific drug binding. *Science*. 323:1718–1722. <https://doi.org/10.1126/science.1168750>
- Amey, J.L., J. Keeley, T. Choudhury, and I. Kuprov. 2021. Neural network interpretation using descrambler groups. *Proc. Natl. Acad. Sci. USA*. 118: e2016917118. <https://doi.org/10.1073/pnas.2016917118>
- Arrigoni, C., A. Rohaim, D. Shaya, F. Findeisen, R.A. Stein, S.R. Nurva, S. Mishra, H.S. Mchaourab, and D.L. Minor Jr. 2016. Unfolding of a temperature-sensitive domain controls voltage-gated channel activation. *Cell*. 164:922–936. <https://doi.org/10.1016/j.cell.2016.02.001>

- Banks, H.T., and M.L. Joyner. 2017. AIC under the framework of least squares estimation. *Appl. Math. Lett.* 74:33–45. <https://doi.org/10.1016/j.aml.2017.05.005>
- Barrett, P.J., Y. Song, W.D. Van Horn, E.J. Hustedt, J.M. Schafer, A. Hadzi-selimovic, A.J. Beel, and C.R. Sanders. 2012. The amyloid precursor protein has a flexible transmembrane domain and binds cholesterol. *Science*. 336:1168–1171. <https://doi.org/10.1126/science.1219988>
- Beechem, J.M. 1992. Global analysis of biochemical and biophysical data. *Methods Enzymol.* 210:37–54. [https://doi.org/10.1016/0076-6879\(92\)10004-W](https://doi.org/10.1016/0076-6879(92)10004-W)
- Beechem, J.M., J.M. Gratton, M. Ameloot, J.R. Knutson, and L. Brand. 1991. The global analysis of fluorescence intensity and anisotropy decay data: second generation theory and programs. In *Topics in Fluorescence Spectroscopy*. J.R. Lakowicz, editor. Plenum Press, New York.
- Borbat, P.P., and J.H. Freed. 2014. Pulse dipolar electron spin resonance: distance measurements. In *Structural Information from Spin-Labels and Intrinsic Paramagnetic Centres in the Biosciences*. C.R. Timmel, and J.R. Harmer, editors. Springer, Berlin. 1–82.
- Bowman, M.K., A.G. Maryasov, N. Kim, and V.J. DeRose. 2004. Visualization of distance distribution from pulsed double electron-electron resonance data. *Appl. Magn. Reson.* 26:23. <https://doi.org/10.1007/BF03166560>
- Brandon, S., A.H. Beth, and E.J. Hustedt. 2012. The global analysis of DEER data. *J. Magn. Reson.* 218:93–104. <https://doi.org/10.1016/j.jmr.2012.03.006>
- Burnham, K.P., and D.R. Anderson. 2002. *Model Selection and Multimodel Inference: A Practical Information-Theoretic Approach*. Second edition. Springer-Verlag, New York.
- Cavanaugh, J.E., and A.A. Neath. 1999. Generalizing the derivation of the Schwarz information criterion. *Commun. Stat. Theory Methods*. 28: 49–66. <https://doi.org/10.1080/03610929908832282>
- Chiang, Y.W., P.P. Borbat, and J.H. Freed. 2005. The determination of pair distance distributions by pulsed ESR using Tikhonov regularization. *J. Magn. Reson.* 172:279–295. <https://doi.org/10.1016/j.jmr.2004.10.012>
- Chufan, E.E., K. Kapoor, and S.V. Ambudkar. 2016. Drug-protein hydrogen bonds govern the inhibition of the ATP hydrolysis of the multidrug transporter P-glycoprotein. *Biochem. Pharmacol.* 101:40–53. <https://doi.org/10.1016/j.bcp.2015.12.007>
- Claxton, D.P., M. Quick, L. Shi, F.D. de Carvalho, H. Weinstein, J.A. Javitch, and H.S. Mchaourab. 2010. Ion/substrate-dependent conformational dynamics of a bacterial homolog of neurotransmitter: sodium symporters. *Nat. Struct. Mol. Biol.* 17:822–829. <https://doi.org/10.1038/nsmb.1854>
- Claxton, D.P., K. Kazmier, S. Mishra, and H.S. Mchaourab. 2015. Navigating membrane protein structure, dynamics, and energy landscapes using spin labeling and EPR spectroscopy. *Methods Enzymol.* 564:349–387. <https://doi.org/10.1016/bs.mie.2015.07.026>
- Claxton, D.P., K.L. Jagessar, P.R. Steed, R.A. Stein, and H.S. Mchaourab. 2018. Sodium and proton coupling in the conformational cycle of a MATE antiporter from *Vibrio cholerae*. *Proc. Natl. Acad. Sci. USA*. 115: E6182–E6190. <https://doi.org/10.1073/pnas.1802417115>
- Collauto, A., H.A. DeBerg, R. Kaufmann, W.N. Zagotta, S. Stoll, and D. Goldfarb. 2017. Rates and equilibrium constants of the ligand-induced conformational transition of an HCN ion channel protein domain determined by DEER spectroscopy. *Phys. Chem. Chem. Phys.* 19:15324–15334. <https://doi.org/10.1039/C7CP01925D>
- Dalmas, O., W. Sandtner, D. Medovoy, L. Frezza, F. Bezanilla, and E. Perozo. 2014. A repulsion mechanism explains magnesium permeation and selectivity in CorA. *Proc. Natl. Acad. Sci. USA*. 111:3002–3007. <https://doi.org/10.1073/pnas.1319054111>
- Dastvan, R., A.W. Fischer, S. Mishra, J. Meiler, and H.S. Mchaourab. 2016. Protonation-dependent conformational dynamics of the multidrug transporter EmrE. *Proc. Natl. Acad. Sci. USA*. 113:1220–1225. <https://doi.org/10.1073/pnas.1520431113>
- Dastvan, R., S. Mishra, Y.B. Peskova, R.K. Nakamoto, and H.S. Mchaourab. 2019. Mechanism of allosteric modulation of P-glycoprotein by transport substrates and inhibitors. *Science*. 364:689–692. <https://doi.org/10.1126/science.aav9406>
- Debruycker, V., A. Hutchin, M. Masureel, E. Ficici, C. Martens, P. Legrand, R.A. Stein, H.S. Mchaourab, J.D. Faraldo-Gómez, H. Remaut, et al. 2020. An embedded lipid in the multidrug transporter LmrP suggests a mechanism for polyspecificity. *Nat. Struct. Mol. Biol.* 27:829–835. <https://doi.org/10.1038/s41594-020-0464-y>
- Dellisanti, C.D., B. Ghosh, S.M. Hanson, J.M. Raspanti, V.A. Grant, G.M. Diarra, A.M. Schuh, K. Satyshur, C.S. Klug, and C. Czajkowski. 2013. Site-directed spin labeling reveals pentameric ligand-gated ion channel gating motions. *PLoS Biol.* 11:e1001714. <https://doi.org/10.1371/journal.pbio.1001714>
- Dürr, K.L., L. Chen, R.A. Stein, R. De Zorzi, I.M. Folea, T. Walz, H.S. Mchaourab, and E. Gouaux. 2014. Structure and dynamics of AMPA receptor GluA2 in resting, pre-open, and desensitized states. *Cell*. 158: 778–792. <https://doi.org/10.1016/j.cell.2014.07.023>
- Edwards, T.H., and S. Stoll. 2016. A Bayesian approach to quantifying uncertainty from experimental noise in DEER spectroscopy. *J. Magn. Reson.* 270:87–97. <https://doi.org/10.1016/j.jmr.2016.06.021>
- Edwards, T.H., and S. Stoll. 2018. Optimal Tikhonov regularization for DEER spectroscopy. *J. Magn. Reson.* 288:58–68. <https://doi.org/10.1016/j.jmr.2018.01.021>
- Edwards, S.J., C.W. Moth, S. Kim, S. Brandon, Z. Zhou, C.E. Cobb, E.J. Hustedt, A.H. Beth, J.A. Smith, and T.P. Lybrand. 2014. Automated structure refinement for a protein heterodimer complex using limited EPR spectroscopic data and a rigid-body docking algorithm: a three-dimensional model for an ankyrin-CDB3 complex. *J. Phys. Chem. B*. 118:4717–4726. <https://doi.org/10.1021/jp4099705>
- Elgeti, M., and W.L. Hubbell. 2021. DEER analysis of GPCR conformational heterogeneity. *Biomolecules*. 11:778. <https://doi.org/10.3390/biom11060778>
- Evans, E.G.B., J.L.W. Morgan, F. DiMaio, W.N. Zagotta, and S. Stoll. 2020. Allosteric conformational change of a cyclic nucleotide-gated ion channel revealed by DEER spectroscopy. *Proc. Natl. Acad. Sci. USA*. 117: 10839–10847. <https://doi.org/10.1073/pnas.1916375117>
- Gamble Jarvi, A., X. Bogetti, K. Singewald, S. Ghosh, and S. Saxena. 2021. Going the dHis-tance: site-directed Cu²⁺ labeling of proteins and nucleic acids. *Acc. Chem. Res.* 54:1481–1491. <https://doi.org/10.1021/acs.accounts.0c00761>
- Georgieva, E.R., P.P. Borbat, C. Ginter, J.H. Freed, and O. Boudker. 2013. Conformational ensemble of the sodium-coupled aspartate transporter. *Nat. Struct. Mol. Biol.* 20:215–221. <https://doi.org/10.1038/nsmb.2494>
- Ghimire, H., E.J. Hustedt, I.D. Sahu, J.J. Inbaraj, R. McCarrick, D.J. Mayo, M.R. Benedikt, R.T. Lee, S.M. Grosser, and G.A. Lorigan. 2012. Distance measurements on a dual-labeled TOAC AChR M28 peptide in mechanically aligned DMPC bilayers via dipolar broadening CW-EPR spectroscopy. *J. Phys. Chem. B*. 116:3866–3873. <https://doi.org/10.1021/jp212272d>
- Göddeke, H., M.H. Timachi, C.A.J. Hutter, L. Galazzo, M.A. Seeger, M. Karttunen, E. Bordignon, and L.V. Schäfer. 2018. Atomistic mechanism of large-scale conformational transition in a heterodimeric ABC exporter. *J. Am. Chem. Soc.* 140:4543–4551. <https://doi.org/10.1021/jacs.7b12944>
- Hilger, D., H. Jung, E. Padan, C. Wegener, K.P. Vogel, H.J. Steinhoff, and G. Jeschke. 2005. Assessing oligomerization of membrane proteins by four-pulse DEER: pH-dependent dimerization of NhaA Na⁺/H⁺ antiporter of *E. coli*. *Biophys. J.* 89:1328–1338. <https://doi.org/10.1529/biophysj.105.062232>
- Hilger, D., Y. Polyhach, E. Padan, H. Jung, and G. Jeschke. 2007. High-resolution structure of a Na⁺/H⁺ antiporter dimer obtained by pulsed electron paramagnetic resonance distance measurements. *Biophys. J.* 93: 3675–3683. <https://doi.org/10.1529/biophysj.107.109769>
- Hustedt, E.J., and A.H. Beth. 1995. Analysis of saturation transfer electron paramagnetic resonance spectra of a spin-labeled integral membrane protein, band 3, in terms of the uniaxial rotational diffusion model. *Biophys. J.* 69:1409–1423. [https://doi.org/10.1016/S0006-3495\(95\)80010-X](https://doi.org/10.1016/S0006-3495(95)80010-X)
- Hustedt, E.J., and A.H. Beth. 1996. Determination of the orientation of a band 3 affinity spin-label relative to the membrane normal axis of the human erythrocyte. *Biochemistry*. 35:6944–6954. <https://doi.org/10.1021/bi9601518>
- Hustedt, E.J., and A.H. Beth. 1999. Nitroxide spin-spin interactions: applications to protein structure and dynamics. *Annu. Rev. Biophys. Biomol. Struct.* 28:129–153. <https://doi.org/10.1146/annurev.biophys.28.1.129>
- Hustedt, E.J., and A.H. Beth. 2001. The sensitivity of saturation transfer electron paramagnetic resonance spectra to restricted amplitude uniaxial rotational diffusion. *Biophys. J.* 81:3156–3165. [https://doi.org/10.1016/S0006-3495\(01\)75952-8](https://doi.org/10.1016/S0006-3495(01)75952-8)
- Hustedt, E.J., and A.H. Beth. 2004. High field/high frequency saturation transfer electron paramagnetic resonance spectroscopy: increased sensitivity to very slow rotational motions. *Biophys. J.* 86:3940–3950. <https://doi.org/10.1529/biophysj.103.035048>
- Hustedt, E.J., C.E. Cobb, A.H. Beth, and J.M. Beechem. 1993. Measurement of rotational dynamics by the simultaneous nonlinear analysis of optical and EPR data. *Biophys. J.* 64:614–621. [https://doi.org/10.1016/S0006-3495\(93\)81420-6](https://doi.org/10.1016/S0006-3495(93)81420-6)

- Hustedt, E.J., A.I. Smirnov, C.F. Laub, C.E. Cobb, and A.H. Beth. 1997. Molecular distances from dipolar coupled spin-labels: the global analysis of multifrequency continuous wave electron paramagnetic resonance data. *Biophys. J.* 72:1861–1877. [https://doi.org/10.1016/S0006-3495\(97\)78832-5](https://doi.org/10.1016/S0006-3495(97)78832-5)
- Hustedt, E.J., F. Marinelli, R.A. Stein, J.D. Faraldo-Gómez, and H.S. Mchaourab. 2018. Confidence analysis of DEER data and its structural interpretation with ensemble-biased metadynamics. *Biophys. J.* 115: 1200–1216. <https://doi.org/10.1016/j.bpj.2018.08.008>
- Ibáñez, L.F., and G. Jeschke. 2019. General regularization framework for DEER spectroscopy. *J. Magn. Reson.* 300:28–40. <https://doi.org/10.1016/j.jmr.2019.01.008>
- Ibáñez, L.F., and G. Jeschke. 2020. Optimal background treatment in pulse dipolar spectroscopy. *Phys. Chem. Chem. Phys.* 22:1855–1868.
- Ibáñez, L.F., G. Jeschke, and S. Stoll. 2020. DeerLab: a comprehensive software package for analyzing dipolar electron paramagnetic resonance spectroscopy data. *Magn. Reson. (Gott.)* 1:209–224. <https://doi.org/10.5194/mr-1-209-2020>
- Jagessar, K.L., D.P. Claxton, R.A. Stein, and H.S. Mchaourab. 2020. Sequence and structural determinants of ligand-dependent alternating access of a MATE transporter. *Proc. Natl. Acad. Sci. USA* 117:4732–4740. <https://doi.org/10.1073/pnas.1917139117>
- Jeschke, G. 2012. DEER distance measurements on proteins. *Annu. Rev. Phys. Chem.* 63:419–446.
- Jeschke, G. 2014. Interpretation of dipolar EPR data in terms of protein structure. In *Structural Information from Spin-Labels and Intrinsic Paramagnetic Centres in the Biosciences*. C.R. Timmel, and J.R. Harner, editors. Springer, Berlin. 83–120.
- Jeschke, G. 2016. Ensemble models of proteins and protein domains based on distance distribution restraints. *Proteins*. 84:544–560. <https://doi.org/10.1002/prot.25000>
- Jeschke, G. 2018a. The contribution of modern EPR to structural biology. *Emerg. Top. Life Sci.* 2:9–18. <https://doi.org/10.1042/ETLS20170143>
- Jeschke, G. 2018b. MMM: A toolbox for integrative structure modeling. *Protein Sci.* 27:76–85. <https://doi.org/10.1002/pro.3269>
- Jeschke, G., V. Chechik, P. Ionita, A. Godt, H. Zimmermann, J. Banham, C.R. Timmel, D. Hilger, and H. Jung. 2006. DeerAnalysis2006—a comprehensive software package for analyzing pulsed ELDOR data. *Appl. Magn. Reson.* 30:473–498. <https://doi.org/10.1007/BF03166213>
- Jin, M.S., M.L. Oldham, Q. Zhang, and J. Chen. 2012. Crystal structure of the multidrug transporter P-glycoprotein from *Caenorhabditis elegans*. *Nature*. 490:566–569. <https://doi.org/10.1038/nature11448>
- Joseph, B., A. Sikora, E. Bordignon, G. Jeschke, D.S. Cafiso, and T.F. Prisner. 2015. Distance measurement on an endogenous membrane transporter in *E. coli* cells and native membranes using EPR spectroscopy. *Angew. Chem. Int. Ed. Engl.* 54:6196–6199. <https://doi.org/10.1002/anie.201501086>
- Joseph, B., E.A. Jaumann, A. Sikora, K. Barth, T.F. Prisner, and D.S. Cafiso. 2019. In situ observation of conformational dynamics and protein ligand-substrate interactions in outer-membrane proteins with DEER/PELDOR spectroscopy. *Nat. Protoc.* 14:2344–2369. <https://doi.org/10.1038/s41596-019-0182-2>
- Kang, Y., X.E. Zhou, X. Gao, Y. He, W. Liu, A. Ishchenko, A. Barty, T.A. White, O. Yefanov, G.W. Han, et al. 2015. Crystal structure of rhodopsin bound to arrestin by femtosecond X-ray laser. *Nature*. 523:561–567. <https://doi.org/10.1038/nature14656>
- Kattinig, D.R., J. Reichenwallner, and D. Hinderberger. 2013. Modeling excluded volume effects for the faithful description of the background signal in double electron-electron resonance. *J. Phys. Chem. B* 117: 16542–16557. <https://doi.org/10.1021/jp408338q>
- Kazmier, K., S. Sharma, S.M. Islam, B. Roux, and H.S. Mchaourab. 2014a. Conformational cycle and ion-coupling mechanism of the Na⁺/hydantoin transporter Mhp1. *Proc. Natl. Acad. Sci. USA* 111:14752–14757. <https://doi.org/10.1073/pnas.1410431111>
- Kazmier, K., S. Sharma, S.M. Islam, B. Roux, H. Weinstein, J.A. Javitch, and H.S. Mchaourab. 2014b. Conformational dynamics of ligand-dependent alternating access in LeuT. *Nat. Struct. Mol. Biol.* 21: 472–479. <https://doi.org/10.1038/nsmb.2816>
- Kim, Y., and J. Chen. 2018. Molecular structure of human P-glycoprotein in the ATP-bound, outward-facing conformation. *Science*. 359:915–919. <https://doi.org/10.1126/science.aar7389>
- Kim, S., S. Brandon, Z. Zhou, C.E. Cobb, S.J. Edwards, C.W. Moth, C.S. Parry, J.A. Smith, T.P. Lybrand, E.J. Hustedt, et al. 2011. Determination of structural models of the complex between the cytoplasmic domain of erythrocyte band 3 and ankyrin-R repeats 13–24. *J. Biol. Chem.* 286: 20746–20757. <https://doi.org/10.1074/jbc.M111.230326>
- Kim, M., S.A. Vishnivetskiy, N. Van Eps, N.S. Alexander, W.M. Cleghorn, X. Zhan, S.M. Hanson, T. Morizumi, O.P. Ernst, J. Meiler, et al. 2012. Conformation of receptor-bound visual arrestin. *Proc. Natl. Acad. Sci. USA* 109:18407–18412. <https://doi.org/10.1073/pnas.1216304109>
- Li, J., K.F. Jaimes, and S.G. Aller. 2014. Refined structures of mouse P-glycoprotein. *Protein Sci.* 23:34–46. <https://doi.org/10.1002/pro.2387>
- Martens, C., R.A. Stein, M. Masureel, A. Roth, S. Mishra, R. Dawaliby, A. Konijnenberg, F. Sobott, C. Govaerts, and H.S. Mchaourab. 2016. Lipids modulate the conformational dynamics of a secondary multidrug transporter. *Nat. Struct. Mol. Biol.* 23:744–751. <https://doi.org/10.1038/nsmb.3262>
- Masureel, M., C. Martens, R.A. Stein, S. Mishra, J.M. Ruysschaert, H.S. Mchaourab, and C. Govaerts. 2014. Protonation drives the conformational switch in the multidrug transporter LmrP. *Nat. Chem. Biol.* 10: 149–155. <https://doi.org/10.1038/nchembio.1408>
- Matsumura, M., J.A. Wozniak, D.P. Sun, and B.W. Matthews. 1989. Structural studies of mutants of T4 lysozyme that alter hydrophobic stabilization. *J. Biol. Chem.* 264:16059–16066. [https://doi.org/10.1016/S0021-9258\(18\)71587-1](https://doi.org/10.1016/S0021-9258(18)71587-1)
- Mchaourab, H.S., P.R. Steed, and K. Kazmier. 2011. Toward the fourth dimension of membrane protein structure: insight into dynamics from spin-labeling EPR spectroscopy. *Structure*. 19:1549–1561. <https://doi.org/10.1016/j.str.2011.10.009>
- Milov, A.D., A.G. Maryasov, and Y.D. Tsvetkov. 1998. Pulsed electron double resonance (PELDOR) and its applications in free-radicals research. *Appl. Magn. Reson.* 15:107–143. <https://doi.org/10.1007/BF03161886>
- Mishra, S., B. Verhalen, R.A. Stein, P.C. Wen, E. Tajkhorshid, and H.S. Mchaourab. 2014. Conformational dynamics of the nucleotide binding domains and the power stroke of a heterodimeric ABC transporter. *eLife*. 3:e02740. <https://doi.org/10.7554/eLife.02740>
- Mittal, A., S. Böhm, M.G. Grütter, E. Bordignon, and M.A. Seeger. 2012. Asymmetry in the homodimeric ABC transporter MsbA recognized by a DARPIn. *J. Biol. Chem.* 287:20395–20406. <https://doi.org/10.1074/jbc.M112.359794>
- Nyenhuis, D.A., T.D. Nilaweera, J.K. Niblo, N.Q. Nguyen, K.H. DuBay, and D.S. Cafiso. 2020. Evidence for the supramolecular organization of a bacterial outer-membrane protein from in vivo pulse electron paramagnetic resonance spectroscopy. *J. Am. Chem. Soc.* 142:10715–10722. <https://doi.org/10.1021/jacs.0c01754>
- Pannier, M., V. Schädler, M. Schöps, U. Wiesner, G. Jeschke, and H.W. Spiess. 2000a. Determination of ion cluster sizes and cluster-to-cluster distances in ionomers by four-pulse double electron electron resonance spectroscopy. *Macromolecules*. 33:7812–7818. <https://doi.org/10.1021/ma000800u>
- Pannier, M., S. Veit, A. Godt, G. Jeschke, and H.W. Spiess. 2000b. Dead-time free measurement of dipole-dipole interactions between electron spins. *J. Magn. Reson.* 142:331–340. <https://doi.org/10.1006/jmre.1999.1944>
- Park, S.-Y., P.P. Borbat, G. Gonzalez-Bonet, J. Bhatnagar, A.M. Pollard, J.H. Freed, A.M. Bilwes, and B.R. Crane. 2006. Reconstruction of the chemotaxis receptor-kinase assembly. *Nat. Struct. Mol. Biol.* 13:400–407. <https://doi.org/10.1038/nsmb1085>
- Paz, A., D.P. Claxton, J.P. Kumar, K. Kazmier, P. Bisignano, S. Sharma, S.A. Nolte, T.M. Liwak, V. Nayak, E.M. Wright, et al. 2018. Conformational transitions of the sodium-dependent sugar transporter, vSGLT. *Proc. Natl. Acad. Sci. USA* 115:E2742–E2751. <https://doi.org/10.1073/pnas.1718451115>
- Pliotas, C., R. Ward, E. Branigan, A. Rasmussen, G. Hagelueken, H. Huang, S.S. Black, I.R. Booth, O. Schiemann, and J.H. Naismith. 2012. Conformational state of the MscS mechanosensitive channel in solution revealed by pulsed electron-electron double resonance (PELDOR) spectroscopy. *Proc. Natl. Acad. Sci. USA* 109:E2675–E2682. <https://doi.org/10.1073/pnas.1202286109>
- Polyhach, Y., A. Godt, C. Bauer, and G. Jeschke. 2007. Spin pair geometry revealed by high-field DEER in the presence of conformational distributions. *J. Magn. Reson.* 185:118–129. <https://doi.org/10.1016/j.jmr.2006.11.012>
- Puljung, M.C., H.A. DeBerg, W.N. Zagotta, and S. Stoll. 2014. Double electron-electron resonance reveals cAMP-induced conformational change in HCN channels. *Proc. Natl. Acad. Sci. USA* 111:9816–9821. <https://doi.org/10.1073/pnas.1405371111>
- Raftery, A.E. 1995. Bayesian model selection in social research. *Sociol. Methodol.* 25:111–163. <https://doi.org/10.2307/271063>
- Raghuraman, H., S.M. Islam, S. Mukherjee, B. Roux, and E. Perozo. 2014. Dynamics transitions at the outer vestibule of the KcsA potassium channel during gating. *Proc. Natl. Acad. Sci. USA* 111:1831–1836. <https://doi.org/10.1073/pnas.1314875111>

- Roser, P., M.J. Schmidt, M. Drescher, and D. Summerer. 2016. Site-directed spin labeling of proteins for distance measurements in vitro and in cells. *Org. Biomol. Chem.* 14:5468–5476. <https://doi.org/10.1039/C6OB00473C>
- Sahu, I.D., E.J. Hustedt, H. Ghimire, J.J. Inbaraj, R.M. McCarrick, and G.A. Lorigan. 2014. CW dipolar broadening EPR spectroscopy and mechanically aligned bilayers used to measure distance and relative orientation between two TOAC spin labels on an antimicrobial peptide. *J. Magn. Reson.* 249:72–79. <https://doi.org/10.1016/j.jmr.2014.09.020>
- Schiemann, O., P. Cekan, D. Margraf, T.F. Prisner, and S.T. Sigurdsson. 2009. Relative orientation of rigid nitroxides by PELDOR: beyond distance measurements in nucleic acids. *Angew. Chem. Int. Ed. Engl.* 48: 3292–3295. <https://doi.org/10.1002/anie.200805152>
- Sen, K.I., T.M. Logan, and P.G. Fajer. 2007. Protein dynamics and monomer-monomer interactions in AntR activation by electron paramagnetic resonance and double electron-electron resonance. *Biochemistry.* 46: 11639–11649. <https://doi.org/10.1021/bi700859p>
- Srivastava, M., and J.H. Freed. 2017. Singular value decomposition method to determine distance distributions in pulsed dipolar electron spin resonance. *J. Phys. Chem. Lett.* 8:5648–5655. <https://doi.org/10.1021/acs.jpcllett.7b02379>
- Srivastava, M., and J.H. Freed. 2019. Singular value decomposition method to determine distance distributions in pulsed dipolar electron spin resonance: II. Estimating uncertainty. *J. Phys. Chem. A.* 123:359–370. <https://doi.org/10.1021/acs.jpca.8b07673>
- Srivastava, M., E.R. Georgieva, and J.H. Freed. 2017. A new wavelet denoising method for experimental time-domain signals: pulsed dipolar electron spin resonance. *J. Phys. Chem. A.* 121:2452–2465. <https://doi.org/10.1021/acs.jpca.7b00183>
- Stein, R.A., E.J. Hustedt, J.V. Staros, and A.H. Beth. 2002. Rotational dynamics of the epidermal growth factor receptor. *Biochemistry.* 41:1957–1964. <https://doi.org/10.1021/bi015733q>
- Stein, R.A., A.H. Beth, and E.J. Hustedt. 2015. A straightforward approach to the analysis of double electron-electron resonance data. *Methods Enzymol.* 563:531–567. <https://doi.org/10.1016/bs.mie.2015.07.031>
- Timachi, M.H., C.A. Hutter, M. Hohl, T. Assafa, S. Böhm, A. Mittal, M.A. Seeger, and E. Bordignon. 2017. Exploring conformational equilibria of a heterodimeric ABC transporter. *eLife.* 6:e20236. <https://doi.org/10.7554/eLife.20236>
- Van Eps, N., L.N. Caro, T. Morizumi, A.K. Kusnetzow, M. Szczepiek, K.P. Hofmann, T.H. Bayburt, S.G. Sligar, O.P. Ernst, and W.L. Hubbell. 2017. Conformational equilibria of light-activated rhodopsin in nanodiscs. *Proc. Natl. Acad. Sci. USA.* 114:E3268–E3275. <https://doi.org/10.1073/pnas.1620405114>
- Van Eps, N., C. Altenbach, L.N. Caro, N.R. Latorraca, S.A. Hollingsworth, R.O. Dror, O.P. Ernst, and W.L. Hubbell. 2018. G_i- and G_s-coupled GPCRs show different modes of G-protein binding. *Proc. Natl. Acad. Sci. USA.* 115:2383–2388. <https://doi.org/10.1073/pnas.1721896115>
- van Veen, H.W. 2001. Towards the molecular mechanism of prokaryotic and eukaryotic multidrug transporters. *Semin. Cell Dev. Biol.* 12:239–245. <https://doi.org/10.1006/scdb.2000.0249>
- van Veen, H.W., M. Putman, A. Margolles, K. Sakamoto, and W.N. Konings. 1999. Structure-function analysis of multidrug transporters in *Lactococcus lactis*. *Biochim. Biophys. Acta.* 1461:201–206. [https://doi.org/10.1016/S0005-2736\(99\)00172-8](https://doi.org/10.1016/S0005-2736(99)00172-8)
- Verhalen, B., R. Dastvan, S. Thangapandian, Y. Peskova, H.A. Koteiche, R.K. Nakamoto, E. Tajkhorshid, and H.S. Mchaourab. 2017. Energy transduction and alternating access of the mammalian ABC transporter P-glycoprotein. *Nature.* 543:738–741. <https://doi.org/10.1038/nature21414>
- Wingler, L.M., M. Elgeti, D. Hilger, N.R. Latorraca, M.T. Lerch, D.P. Staus, R.O. Dror, B.K. Kobilka, W.L. Hubbell, and R.J. Lefkowitz. 2019. Angiotensin analogs with divergent bias stabilize distinct receptor conformations. *Cell.* 176:468–478.e11. <https://doi.org/10.1016/j.cell.2018.12.005>
- Worswick, S.G., J.A. Spencer, G. Jeschke, and I. Kuprov. 2018. Deep neural network processing of DEER data. *Sci. Adv.* 4:eaat5218. <https://doi.org/10.1126/sciadv.aat5218>
- Yee, E.F., R.P. Diensthuber, A.T. Vaidya, P.P. Borbat, C. Engelhard, J.H. Freed, R. Bittl, A. Möglich, and B.R. Crane. 2015. Signal transduction in light-oxygen-voltage receptors lacking the adduct-forming cysteine residue. *Nat. Commun.* 6:10079. <https://doi.org/10.1038/ncomms10079>
- Zhou, Z., S.C. DeSensi, R.A. Stein, S. Brandon, M. Dixit, E.J. McArdle, E.M. Warren, H.K. Kroh, L. Song, C.E. Cobb, et al. 2005. Solution structure of the cytoplasmic domain of erythrocyte membrane band 3 determined by site-directed spin labeling. *Biochemistry.* 44:15115–15128. <https://doi.org/10.1021/bi050931t>
- Zhu, S., R.A. Stein, C. Yoshioka, C.H. Lee, A. Goehring, H.S. Mchaourab, and E. Gouaux. 2016. Mechanism of NMDA receptor inhibition and activation. *Cell.* 165:704–714. <https://doi.org/10.1016/j.cell.2016.03.028>

Supplemental material

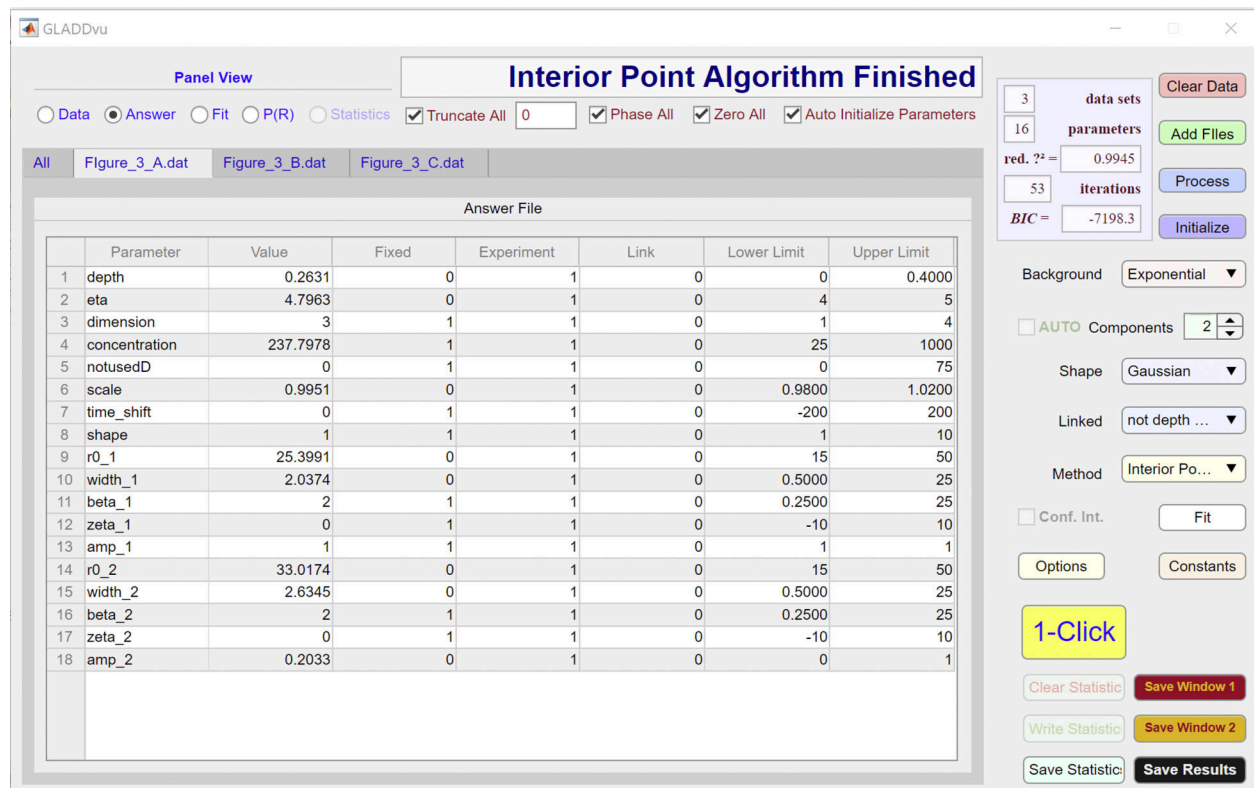


Figure S1. Screenshot of the answer panel for dataset A of GLADDvu during the global analysis of simulated data using model 3. Related to Table 4 and Fig. 4 D.

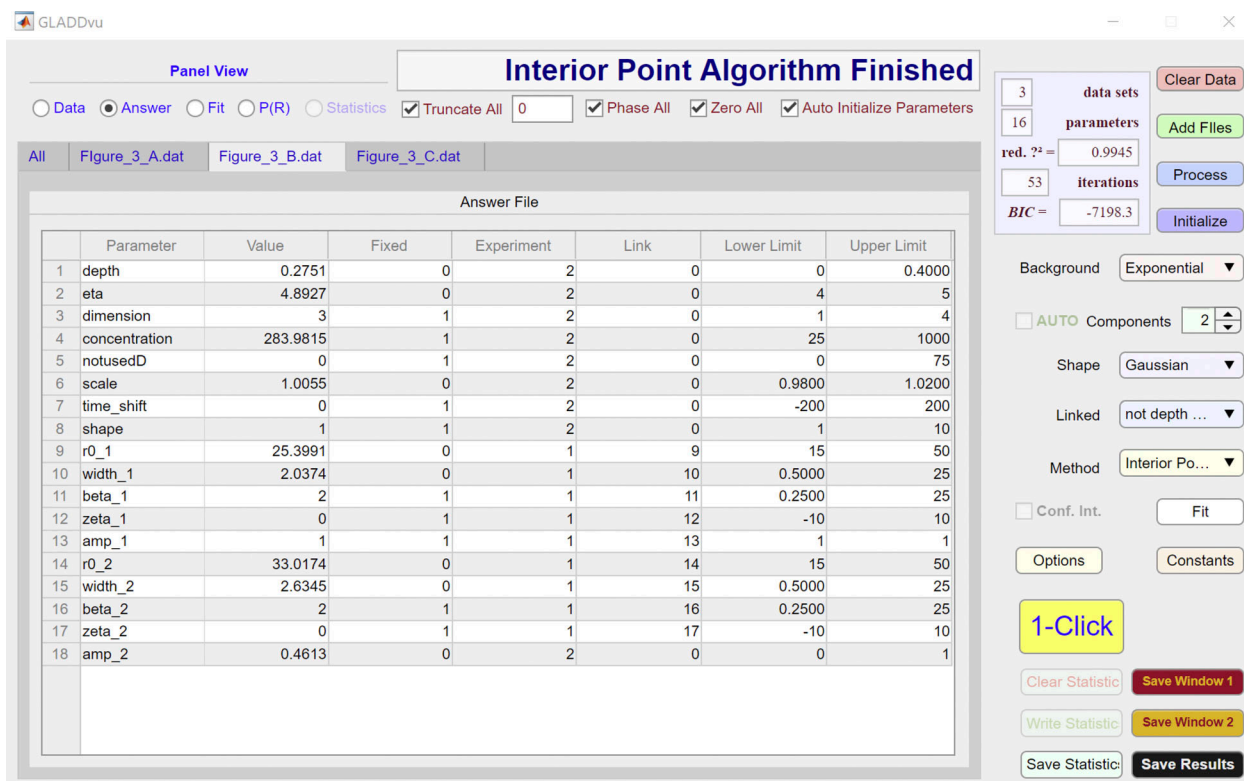


Figure S2. Screenshot of the answer panel for dataset B of GLADDvu during the global analysis of simulated data using model 3. Related to Table 4 and Fig. 4 D.

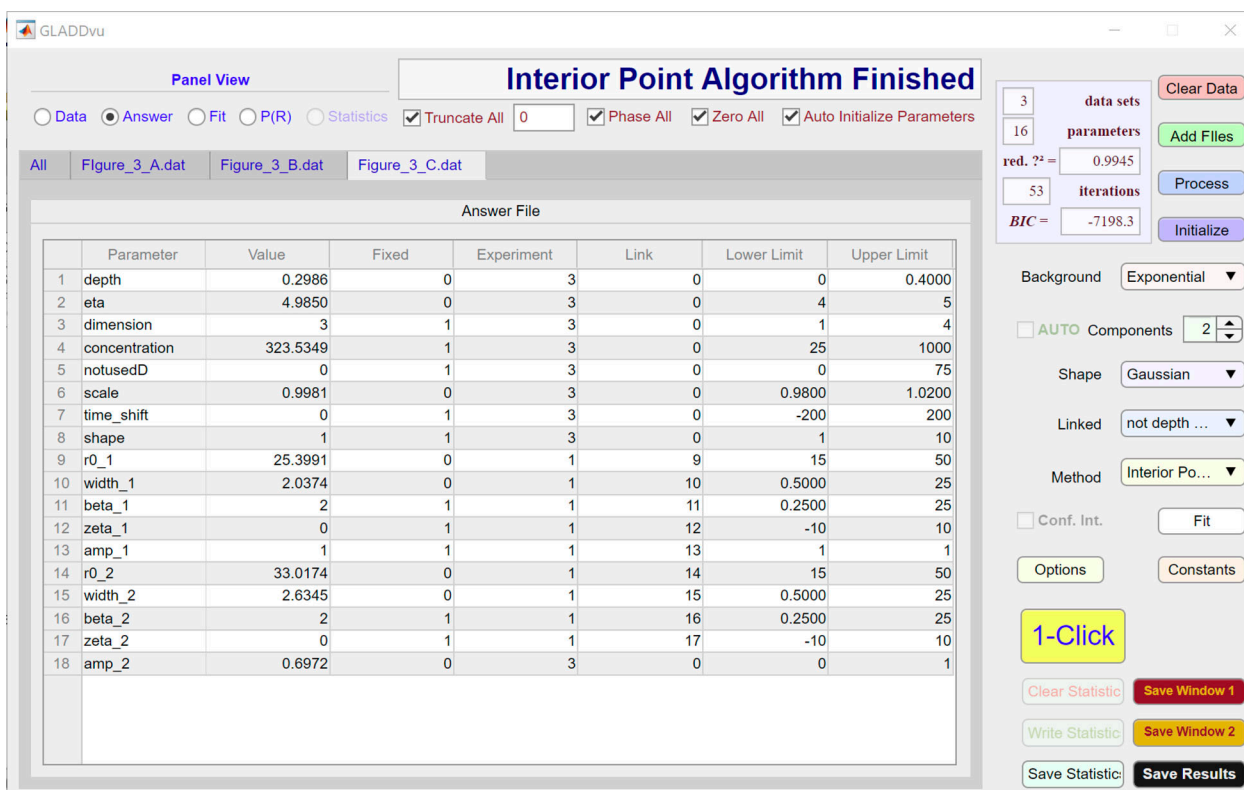


Figure S3. Screenshot of the answer panel for dataset C of GLADDvu during the global analysis of simulated data using model 3. Related to Table 4 and Fig. 4 D.

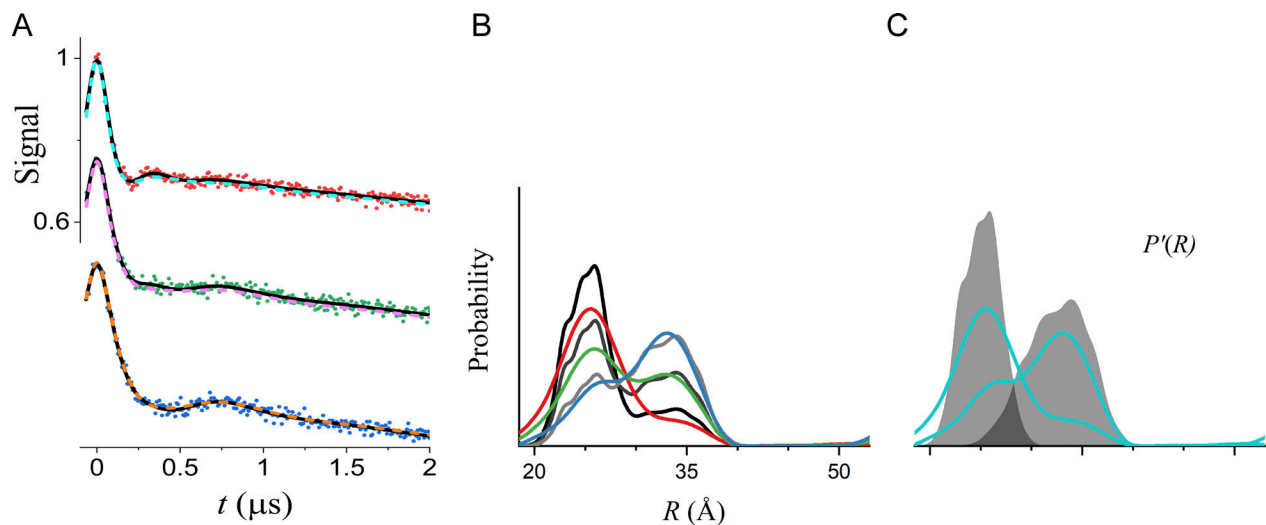


Figure S4. **Global analysis of the same simulated DEER data as in Fig. 4 using Tikhonov regularization.** (A) The data are shown as filled circles. The best-fit lines for model 3 (R_0 and σ_R values linked) are shown as solid black lines. The dashed colored lines were obtained using DeerLab version 0.13.2 (Ibáñez et al., 2020) to perform a global analysis using nonparametric distance distributions based on Tikhonov regularization. (B) $P(R)$ from DeerLab for datasets A (red), B (green), and C (blue). The black lines are the true $P(R)$ used for the simulations. (C) The $P'(R)$ of the underlying components of the global analysis obtained from DeerLab are shown in cyan, and the true $P'(R)$ used for the simulations are superimposed as shaded regions. The global Tikhonov fit with unconstrained fractions of the conformations does not recover the proper distributions of the hypothetical pure conformational states if traces representing the pure conformations are not included in the data. The model-based approach (Fig. 4) does recover the pure conformational states because it favors $P'(R)$ with a minimum number of components. If applicable, a chemical equilibrium model and Tikhonov regularization, as is possible with DeerLab, effectively constrains the mole fractions and can recover the true $P'(R)$.

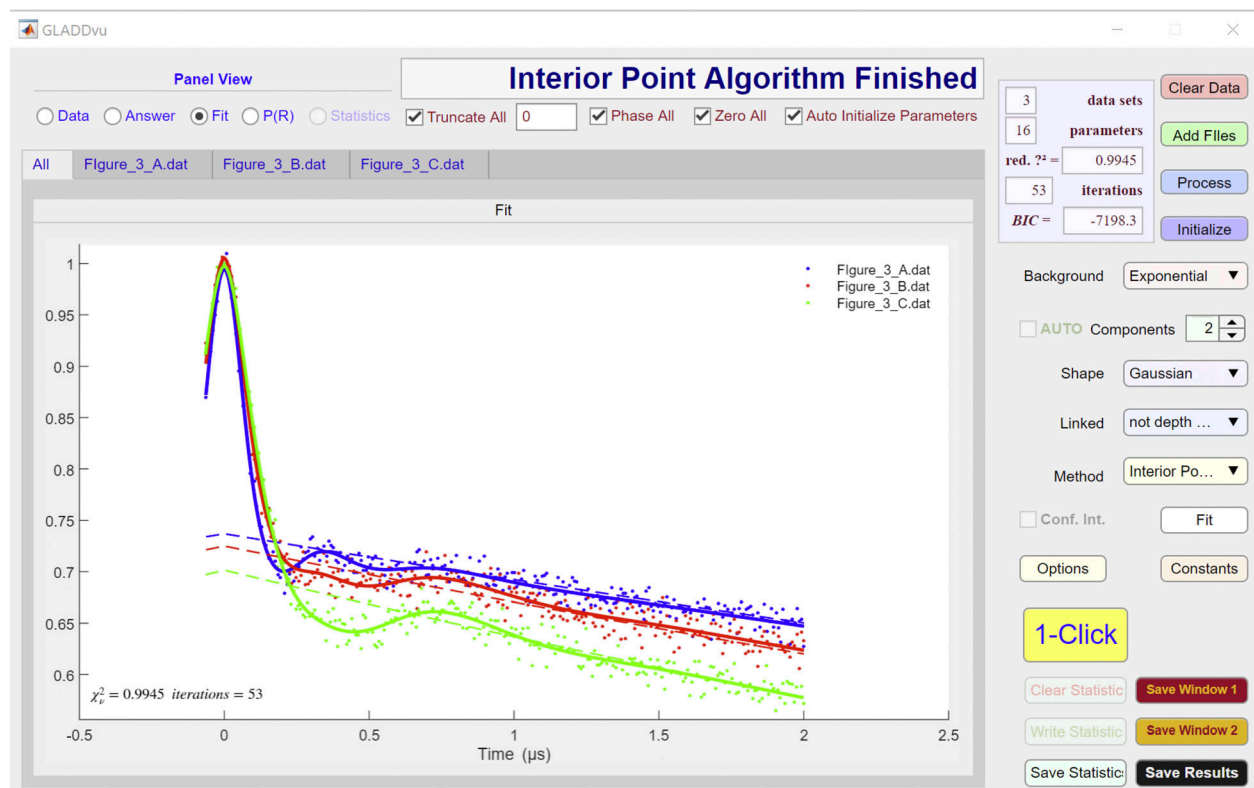


Figure S5. **Screenshot of the fit panel of GLADDvu during the global analysis of simulated data using model 3.** Related to Table 4 and Fig. 4 D.

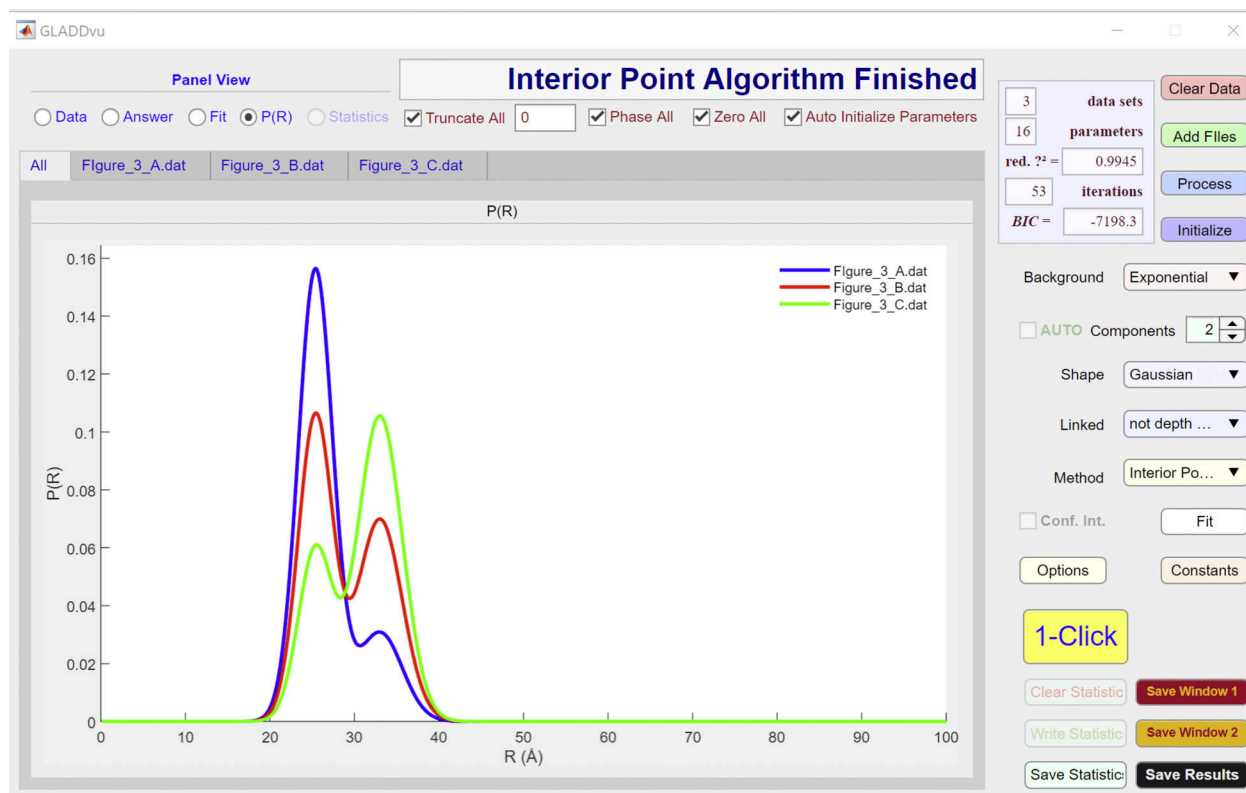


Figure S6. Screenshot of the $P(R)$ panel of GLADDvu during the global analysis of simulated data using model 3. Related to Table 4 and Fig. 4 D.

A Tikhonov Regularization

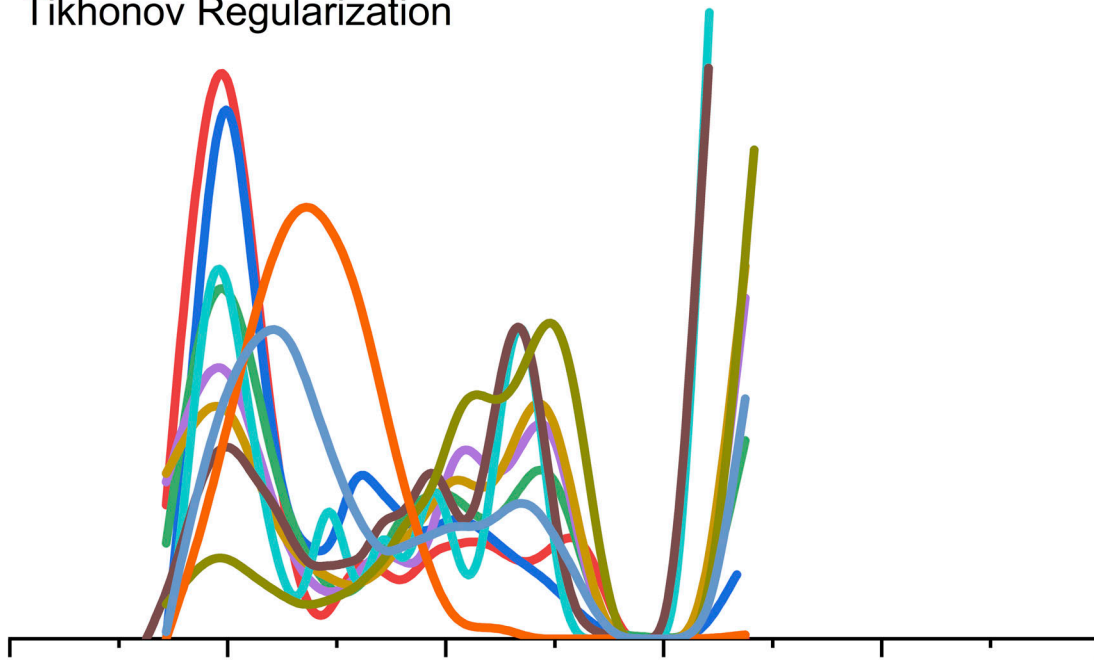
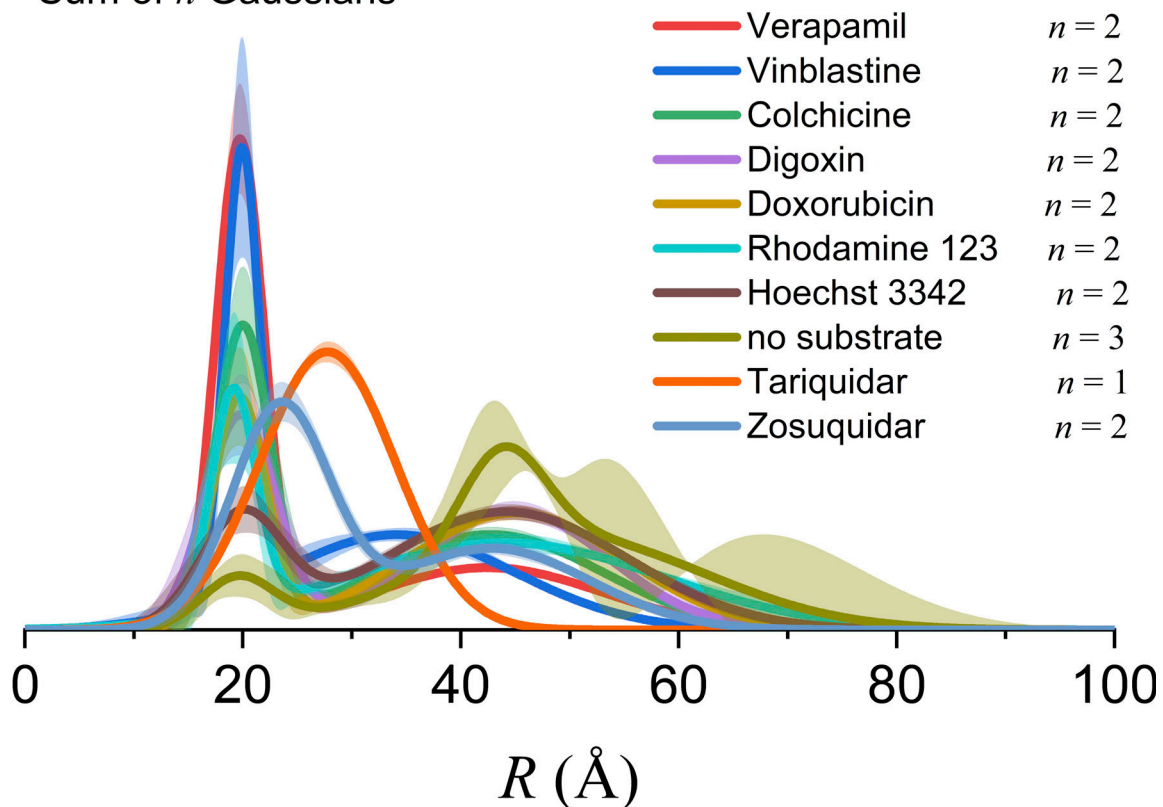
B Sum of n Gaussians

Figure S7. **Distance distributions from individual fits to the DEER data for Pgp in Fig. 6.** (A) The model-free $P(R)$ were obtained using Tikhonov regularization in DeerAnalysis 2019 (Jeschke et al., 2006). The optimal regularization factor was determined by generalized cross-validation and the starting time point for background fitting using the validation tool. (B) The model-based $P(R)$ were obtained assuming a 3-D exponential background and using Gaussian components in DD (Brandon et al., 2012; Stein et al., 2015; Hustedt et al., 2018). The optimal number of Gaussians, n , was determined using BIC values.

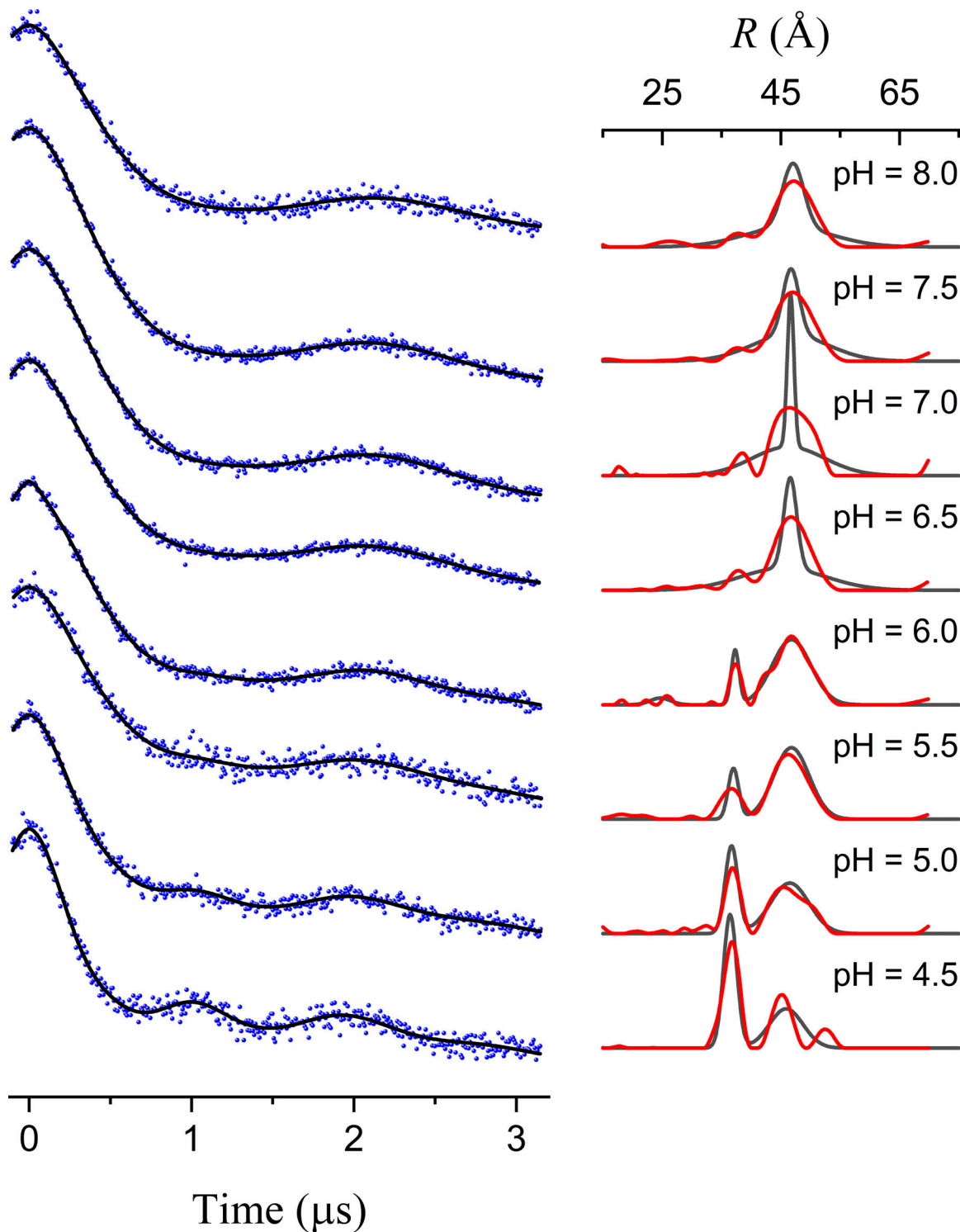


Figure S8. **Results from individual fits for LmrP data in Fig. 8.** On the left, the data are shown as black dots with the individual model-based fits as blue lines. The corresponding $P(R)$ are shown (black lines) on the right together with those obtained from Tikhonov regularization using DeerAnalysis 2019 (Jeschke et al., 2006; red lines). The widths of the narrow components at pH 6.5 and 7.0 have large relative uncertainties, $\sigma_r = 1.1 \pm 1.1$ Å and $\sigma_r = 0.6 \pm 2.6$ Å, owing to the fact that the modulation is not fully damped over the measured evolution time.

Video 1. **Demonstration of the use of DD (<https://github.com/erichustedt/DD>) to perform the model-based fits of a T4L dataset.** The fits listed in Table 1 and Table 2 using $n = 1, 2$, and 3 Gaussians are performed using DD. The optimal results, as determined by BIC values, were obtained for $n = 2$ and are shown in Fig. 2. The dataset (T4L065-080M_08) is available for download.

Video 2. **Demonstration of the use of GLADDvu (<https://github.com/erichustedt/GLADDvu>) to perform the model-based fits of a T4L dataset.** The fits listed in Table 1 and Table 2 using $n = 1, 2$, and 3 Gaussians are performed using GLADDvu. The optimal results, as determined by BIC values, were obtained for $n = 2$ and are shown in Fig. 2. The dataset (T4L065-080M_08) is available for download.

Video 3. **Demonstration of the use of GLADDvu (<https://github.com/erichustedt/GLADDvu>) to perform the model-based global analysis of three simulated datasets.** The fits to the six different models listed in Table 4 are performed. The optimal results, as determined by BIC values, were obtained for model 3 and are shown in Fig. 4. The datasets (Fig. 4, A–C) are available for download.

Video 4. **Demonstration of the use of GLADDvu (<https://github.com/erichustedt/GLADDvu>) to perform the model-based global analysis of the Pgp datasets.** The fits to the three different models listed in Table 5 are performed. The optimal results, as determined by BIC values, were obtained for model 2 and are shown in Fig. 6.